Journal of Non-Newtonian Fluid Mechanics 292 (2021) 104524

Contents lists available at ScienceDirect

Journal of Non-Newtonian Fluid Mechanics

journal homepage: www.elsevier.com/locate/jnnfm

A new approach for modeling viscoelastic thin film lubrication

Humayun Ahmed, Luca Biancofiore *

Mechanical Engineering Department, Bilkent University, 06800, Ankara, Turkey

ARTICLE INFO

Keywords:
Lubrication theory
Viscoelasticity
Thin films
Tribology

ABSTRACT

Lubricants can exhibit significant viscoelastic effects due to the addition of high molecular weight polymers. The overall behavior of the mixture is vastly different from a simpler Newtonian fluid. Therefore, understating the influence of viscoelasticity on the load carrying capacity of the film is essential for lubricated contacts. A new modeling technique based on lubrication theory is proposed to take into account viscoelastic effects. As a result, we obtain a modified equation for the pressure, i.e. the viscoelastic Reynolds (VR) equation. We have first examined a parabolic slider to mimic a roller bearing configuration. An increase of the load carrying capacity is observed when polymers are added to the lubricant. Furthermore, our results are compared with existing models based on the lubrication approximation and direct numerical simulations (DNS). For small Weissenberg number (Wi), i.e. the ratio between the polymer relaxation time and the residence time scale, VR predicts the same pressure of the linearized model, in which ϵWi is the perturbation parameter (ϵ is the ratio between the vertical length scale and the horizontal length scale). However, the difference grows rapidly as viscoelastic effects become stronger. Excellent quantitative and qualitative agreement is observed between DNS and our model over small to moderate Weissenberg number. While DNS is numerically unstable at high values of the Weissenberg number, VR does not have the same issue allowing to capture the evolution of the stress and pressure also when the viscoelastic effects are strong. It is shown that even in high shear flows, normal stresses have the largest impact on load carrying capacity and thus cannot be neglected. Furthermore, the additional pressure due to viscoelasticity comprises two components, the first one due to the normal stress and the second one due to the shear stress. Afterwards, the methodology used for the parabolic slider is extended to a plane slider where, instead, the load decreases by adding polymers to the fluid. In particular, under the effect of the polymers surface slopes enhance the rate at which pressure gradients increase, whereas curvature opposes this along the contact. Therefore, the increase of the load carrying capacity observed for viscoelastic lubricants is due to its shape close to the inlet, which is steeper than the plane slider.

1. Introduction

Lubrication is essential for the proper functioning of the mechanical components susceptible to degradation due to friction and wear. Surface friction is in general an undesirable effect and leads to an excessive energy consumption. Additionally, excessive loading of surfaces leads to unwanted contact between the sliding surfaces and possibly failure. Therefore, lubricants are carefully designed and selected in order to satisfy the load carrying capacity and other aspects specific to their application. Lubrication theory and models used to evaluate pressure, stress and velocity in lubricated contacts have evolved greatly over the years. While Newtonian lubricants are rather well understood under lubrication theory primarily because the underlying governing equations are well defined [1,2], more complex non-linear rheological effects still need to be fully unveiled, such as the variation of viscosity against pressure and temperature or non-Newtonian effects.

The addition of polymers as viscous enhancers in lubricants to increase the load carrying capacity is a common practice. However strong non-Newtonian effects can occur due to this addition. For instance polymeric lubricants were observed to present shear thinning effects [3,4]. Another important non-Newtonian effect related with polymers is viscoelasticity, which in the Tribology community has received much less attention than shear thinning. It can manifest strongly in polymeric lubricants if the Weissenberg number (Wi), i.e the ratio between the polymer relaxation time and polymer deformation time scale, is large enough. There is ample experimental and numerical evidence that load enhancement occurs due to the elasticity of the lubricant [5,6]. The general focus in lubrication has been towards shear thinning effects as a result of the large shear stresses but evidences also suggest that the normal stress gradients cannot be neglected [7,8].

* Corresponding author.
E-mail address: luca@bilkent.edu.tr (L. Biancofiore).
URL: https://web4.bilkent.edu.tr/fluidframe/ (L. Biancofiore).

https://doi.org/10.1016/j.jnnfm.2021.104524
Received 3 November 2020; Received in revised form 8 March 2021; Accepted 9 March 2021
Available online 27 March 2021

The continuum description of the polymers provides both explicit and implicit constitutive equations that can capture the transport of polymeric stress. For example, an explicit model is the Oldroyd-B constitutive equation [9]. This model assumes constant viscosity and describes the transport via a convective–derivative. Non-linear constitutive models include Phan–Thien–Tanner (PTT) [10,11] and FENE type models [12,13] for example. These models are able to predict a wide range of phenomena associated with viscoelasticity, ranging from the onset of so-called elastic instabilities [14] to the polymers influence on turbulence transition [15]. However, there is a need of robust numerical methods to solve the equations coupled with these constitutive relations.

The most reliable continuum based solutions to the viscoelastic problem will come from the direct numerical solution of the Navier–Stokes equations coupled non-linearly with a valid constitutive relation. Unfortunately a strong non-linear instability, not immediately noticeable from the governing equations, appears. The problem is termed as the high Weissenberg number problem (HWNP) and it emerges as soon as Wi becomes large. There is no strict mathematical definition of 'large' and it varies based on the nature of the problem. One of the reasons postulated for this instability is the failure of the polynomial based numerical schemes to accurately capture the exponential gradients of stress [16]. A direct result of which is that the conformation tensor ceases to remain symmetric positive definite (SPD). This failure leads to a larger growth rate of the stress and the inability of the advective terms to remove stress effectively. Therefore, numerically we have a net accumulation of stress which inhibits convergence. The first remedy was offered by a transformation of the conformation tensor into a logarithmic variable that converts the ordinary polynomial difference schemes to an exponential one. The approach is termed as the Log-Conformation-Representation (LCR) [16]. Higher order schemes can be constructed and applied via the LCR [17] and different spatial discretization techniques are also possible [18]. The first open source implementation was made available in OpenFoam [19] by Habla et al. [20]. Details regarding the efficiency of the numerical schemes, discretization and performance metrics can be found in the original work of the authors.

Due to this numerical complexity, only simplified models are available in literature for lubricated contacts in which the necessary assumptions restrict their use to weakly viscoelastic lubricants. The first non-linear approach towards viscoelasticity in thin lubricating films under pure rolling was conducted by Dowson [21] who derived a generalized Reynolds (GR) equation. This model had the capacity to include several rheological phenomena. Later it was shown that the model can be greatly simplified under certain assumptions and coupled with upper convective Maxwell [22,23]. Firstly, the normal stress of the polymers was neglected in the momentum equations and only effects due to shear stresses were considered. This is well suited for a shear thinning fluid where it is assumed that viscosity becomes very small for high shear rates. Secondly, if the surface slope is small, then only the material derivative of the stress bears importance. The first GR-based study to understand viscoelasticity in lubrication was by Peiran and Shizhu [24] followed by Wolff and Kubo [25]. However, their analyses were coupled with thermal and shear thinning effects. Although GR can accurately describe effects that vary along the film thickness such as viscosity dependence on temperature and shear stress, there is no conclusive evidence about its usefulness for purely viscoelastic cases. Other similar constraints on the constitutive relations involved truncating all the spatial differential operators entirely and only retaining the time derivative only albeit under very specific conditions of low polymer relaxation time and high shear rates [26]. An alternative formulation for PTT was proposed by Akyildiz and Bellout [27] in which the normal stress is not neglected. However in their model, they omit completely the material derivative in the polymer constitutive equations retrieving that the shear stress is linear along the wall-normal direction (as in GR).

The first linearized viscoelastic model for lubrication under pure sliding was developed by Tichy [28]. The starting point for such an approach is the reduced set of momentum equations obtained via the thin film approximation. A key point to note is that normal stresses are retained and the scaling factors under the thin film approximation are obtained from the constitutive relation. The velocity and pressure fields are up to the first order by using the Deborah number, i.e. the ratio between the polymer relaxation time and residence time, as perturbation parameters [29–31]. Note that the Deborah number is related to the Weissenberg number, for the lubricated contact by the thin film parameter $\epsilon = \frac{h_0}{\ell}$, i.e. $De = \epsilon Wi$, where h_0 and ℓ are the vertical and horizontal length scales, respectively. Li [32] also found the second order solution in the thin film parameter. This expansion in De, after some simplifications and algebraic manipulations, gives the De-order velocity and pressure fields. Additionally, linearized solutions prove highly useful in analyzing different constitutive laws such as PTT or FENE-P [33] which are generally non-linear in the stress.

While the linearized models can be accurate only at low Wi, the assumptions made in GR to simplify the equations in order to avoid numerical instabilities are too strict. This limits the range of parameters in which accurate results are obtained to a narrow region. Therefore there is a need of models that are (i) able to describe the non-linear behavior of viscoelastic lubricants in pure sliding contacts at moderate and large Weissenberg numbers without omitting any terms in the polymer constitutive equations (as in GR or in Akyildiz and Bellout [27]) and (ii) flexible enough to account for changes in the constitutive equation. In this study, we address this issue by proposing a new approach based on the fundamental lubrication theory. The paper is organized as follows, in Section 2 we briefly describe the available models and introduce a new model, i.e. the viscoelastic Reynolds (VR) equation. In Section 3 we compare VR against existing models and the direct numerical simulation (DNS) in modeling a parabolic slider, while in Section 4 we extend the analysis to a plane slider. Section 5 presents a discussion regarding the contrasting results between the parabolic and plane slider. Finally, conclusions are drawn in Section 6 based on our findings.

2. Models

This section is organized as follows. We will first introduce the thin film equations for viscoelastic lubrication in Section 2.1. Afterwards we describe the channel geometry in Section 2.2. In Section 2.3, a summary of the available models is presented, while in Section 2.4 we briefly illustrate the methodology behind the direct numerical simulations of viscoelastic lubricants. Finally, in Section 2.5 we describe the viscoelastic Reynolds equation developed in this paper.

2.1. Lubrication theory

We will start with the dimensional Navier–Stokes equations coupled with the Oldroyd-B constitutive equation for the polymers,

$$\nabla \cdot \mathbf{u}^* = 0, \tag{1a}$$

$$\frac{D}{Dt}(\mathbf{u}^*) = -\nabla p^* + \eta_s \nabla^2 \mathbf{u}^* + \nabla \cdot \boldsymbol{\tau}^* \quad \text{and} \tag{1b}$$

$$\boldsymbol{\tau}^* + \lambda \left(\frac{D\boldsymbol{\tau}^*}{Dt^*} - \mathbf{L}^* \boldsymbol{\tau}^* - \boldsymbol{\tau}^* \mathbf{L}^{*T} \right) = 2\eta_p \mathbf{D}^*, \tag{1c}$$

where t^* is the time, $\mathbf{u}^*(u^*, v^*)$ is the velocity vector, p^* is the scalar pressure, η_s is the solvent viscosity, $\boldsymbol{\tau}^*$ is the polymeric stress tensor, η_p is the polymer viscosity, $\mathbf{L}^*$ is the velocity gradient tensor, $\mathbf{D}^*$ is the deformation tensor and λ is the polymer relaxation time. Note that the x^* and y^* represent the horizontal and vertical directions, respectively.

In this work we assume that the entrance height of the channel h_0 is smaller than its length ℓ ($h_0 \ll \ell$). For this reason we can use a thin film approximation to simplify the governing equations.

The appropriate non-Newtonian scaling factors are obtained from the constitutive relation [28,34],

$$\begin{aligned} x &= \frac{x^*}{\ell}, & y &= \frac{y^*}{h_0}, & u &= \frac{u^*}{U}, \\ v &= \frac{v^*}{\epsilon U}, & \epsilon &= \frac{h_0}{\ell}, & t &= t^* \frac{U}{h_0}, \\ \tau_{xx} &= \tau^*_{xx} \frac{h_0^2}{(\eta_s+\eta_p)U\ell}, & \tau_{xy} &= \tau^*_{xy} \frac{h_0}{(\eta_s+\eta_p)U}, & & \\ \tau_{yy} &= \tau^*_{yy} \frac{\ell}{(\eta_s+\eta_p)U}, & p &= (p^* - p_0)\frac{h_0^2}{(\eta_s+\eta_p)U\ell}, & & \end{aligned} \tag{2}$$

where U is the reference velocity. Note that the flow time scale is measured using the vertical length scale h_0 instead of the horizontal length scale ℓ as in previous studies [27,28]. The definition of the dimensionless scalar components of the polymer stress is commonly found in literature pertaining to viscoelastic thin films [35]. We substitute the scaling defined in Eq. (2) into the governing equations (Eqs. (1)) and eliminate the terms on the order of $O(\epsilon^2)$ to obtain the thin film equations,

$$\frac{\partial u}{\partial x} + \frac{\partial v}{\partial y} = 0, \tag{3a}$$

$$\frac{\partial p}{\partial x} = \beta \frac{\partial^2 u}{\partial y^2} + \frac{\partial \tau_{xy}}{\partial y} + \frac{\partial \tau_{xx}}{\partial x}, \tag{3b}$$

$$\frac{\partial p}{\partial y} = 0, \tag{3c}$$

$$\tau_{xx} + \epsilon Wi\left(\frac{D\tau_{xx}}{Dt} - 2\tau_{xy}\frac{\partial u}{\partial y} - 2\tau_{xx}\frac{\partial u}{\partial x}\right) = 0, \tag{3d}$$

$$\tau_{xy} + \epsilon Wi\left(\frac{D\tau_{xy}}{Dt} - \tau_{yy}\frac{\partial u}{\partial y} - \tau_{xx}\frac{\partial v}{\partial x}\right) = (1-\beta)\frac{\partial u}{\partial y}, \tag{3e}$$

$$\tau_{yy} + \epsilon Wi\left(\frac{D\tau_{yy}}{Dt} - 2\tau_{xy}\frac{\partial v}{\partial x} - 2\tau_{yy}\frac{\partial v}{\partial y}\right) = 2(1-\beta)\frac{\partial v}{\partial y}, \tag{3f}$$

where $Wi = \lambda U/h_0$ and $\beta = \eta_s/(\eta_s + \eta_p)$ is the solvent viscosity concentration. Note that in this paper if not specified otherwise we set $\beta = 0.8$. We would like to emphasize that the terms on the ϵWi-order cannot be eliminated since we assume that the Weissenberg number is large [27]. Finally, in this paper we will focus on the final steady-state solution.

2.2. Geometry

In this study, we focus on two particular geometries: (i) a parabolic slider and (ii) a plane slider, see Fig. 1a and Fig. 1b, respectively. We choose a parabolic surface because is common for contact problems in tribological applications since it represents a good approximation of the contact region in bearings, gears and mechanical components in general. The non-dimensional surface height for the parabolic slider is defined by,

$$h(x) = 4(1-\alpha)x^2 + 4(\alpha-1)x + 1, \tag{4}$$

where $\alpha = h_{min}/h_{max}$ denotes the aspect ratio, i.e. the ratio of the minimum and maximum height within the channel. We assume the parabolic slider is externally pressurized and cavitation does not occur in the diverging portion of the channel. The plane slider approximates a thrust pad which is important for heavy machinery in several industrial applications. Its surface height is defined by

$$h(x) = 1 - (1-\alpha)x. \tag{5}$$

For both geometries the top surface is stationary while the bottom surface is moving. Since there is no vertical motion of the top or bottom surface, our configuration is described as pure sliding. Note that we have chosen the velocity of the lower boundary as reference velocity, i.e $u(x,0) = 1$.

There is a general debate regarding the appropriate set of pressure boundary conditions in the viscoelastic limit for lubricated contacts. Arguments available in literature suggest imposing conditions on the total stress tensor, rather than just the pressure. We refer the reader to the discussion available in Tanner [36], Tichy and Bou-Saïd [37] and, with more details, in Sawyer and Tichy [38].

In our work, the pressure at the boundaries of the film is expressed as a combination of the normal stresses

$$p^* = \theta(\tau^*_{xx} - \tau^*_{yy}), \tag{6}$$

where θ is a dimensionless scalar so that $0 \le \theta \le 1$. Substituting in Eq. (6) the scaling factors of Eq. (2) we obtain

$$p = \theta(\tau_{xx} - \epsilon^2 \tau_{yy}). \tag{7}$$

For small ϵ, (7) becomes $p = \theta\tau_{xx}$. Thus, it is equivalent to set the pressure equal to a linear function in θ of the normal stress along the flow direction. However, we must use the average stress $\bar{\tau}_{xx} = \int_0^h \tau_{xx} dy$, since the pressure cannot vary across the channel at any x (see Eq. (3c)). Therefore, we set at the film boundaries

$$p = \theta\bar{\tau}_{xx}. \tag{8}$$

There are two limiting cases for the boundary conditions depending on the value of θ

1. $\theta = 0$. This case corresponds to set the pressure equal to the Newtonian boundary condition

   $$p = 0. \tag{9}$$

   In this scenario we assume that the film is Newtonian at two extremities. For this reason we refer to Eq. (9) as the Newtonian boundary condition. Note that Eq. (9) is equivalent to what Sawyer and Tichy [38] call the load carrying boundary condition.
2. $\theta = 1$. In this case we set the average normal stress along the flow direction equal to the pressure

   $$p = \bar{\tau}_{xx}. \tag{10}$$

   We refer to Eq. (10) as the normal stress boundary condition.

We would like to highlight that the most appropriate range of values of θ is not known. The two limiting cases (i.e Newtonian and the normal stress boundary conditions) are clearly contrasting and give different results. However, it is not the aim of this study to discuss the validity of these boundary conditions leaving it as potential future work.

2.3. Available models

There are two simplified models available for viscoelastic lubricants: (i) the generalized Reynolds equation (see Section 2.3.1) and (ii) the linearized viscoelastic Reynolds equation (see Section 2.3.2). We present a modified version of the two models since we use Oldroyd-B as constitutive equation, whereas the previous works focused on the upper-convected Maxwell (UCM) model. The difference is that the solvent viscosity concentration β is taken into account in our modified approach.

2.3.1. Generalized Reynolds equation (GR)

More details regarding the explicit derivation of GR can be found in Wolff and Kubo [25] for a general flow across a thin lubricated contact. We obtain the parent equations that are used to derive GR from Eqs. (3a)–(3f) by assuming that $\tau_{xx} = 0$ and $\tau_{yy} = 0$. We present the final form in terms of the solvent viscosity concentration β,

$$\begin{aligned} \frac{d}{dx}\left(\frac{h^3}{12}\frac{dp}{dx}\right) &= \frac{1}{2}\frac{dh}{dx} \\ &+ \epsilon Wi \frac{d}{dx}\left(-\int_0^h \frac{y}{h}\int_0^h \frac{D\tau_{xy}}{Dt}dy'dy + \int_0^h \int_0^y \frac{D\tau_{xy}}{Dt}dy'dy\right), \end{aligned} \tag{11a}$$

$$\tau_{xy} + \epsilon Wi \frac{D\tau_{xy}}{Dt} = (1-\beta)\frac{\partial u}{\partial y}, \tag{11b}$$

$$\frac{D\tau_{xy}}{Dt} = \frac{\partial \tau_{xy}}{\partial t} + u\frac{\partial \tau_{xy}}{\partial x}. \tag{11c}$$

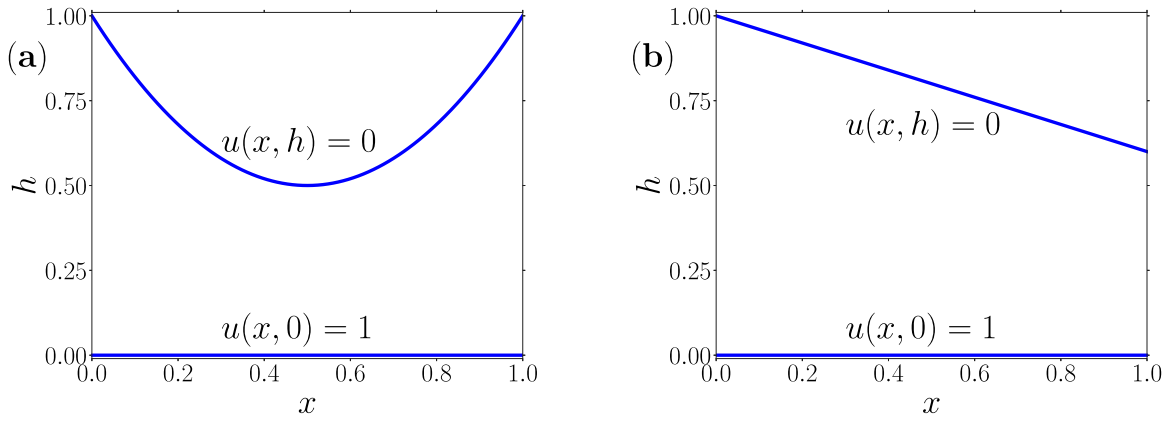

Fig. 1. (a) The parabolic slider for $\alpha = 0.5$ and (b) the plane slider for $\alpha = 0.6$.

Table 1
The boundary conditions for the (i) velocity, (ii) pressure and (iii) polymer stress applied to the GR. N/A stands for not applicable. Note that for GR we are forced to use the Newtonian boundary condition for the pressure at the film extremities since τ_{xx} is neglected.

Boundary	$x=0$	$x=1$	$y=0$	$y=h(x)$
p	$p=0$	$p=0$	N/A	N/A
$\mathbf{u}$	N/A	N/A	$\mathbf{u}=(1,0)$	$\mathbf{u}=(0,0)$
$\boldsymbol{\tau}$	$(\nabla\boldsymbol{\tau})\cdot\mathbf{n}=0$	$(\nabla\boldsymbol{\tau})\cdot\mathbf{n}=0$	N/A	N/A

Table 1 summarizes the boundary conditions for the pressure and the stress for GR. Note that GR requires an update to the horizontal velocity field at each time step.

2.3.2. Linearized viscoelastic Reynolds equation (LIN)

The linearized model is derived via a perturbation analysis. The scalar components of $\mathbf{u}$ and $\boldsymbol{\tau}$, and p are expressed in terms of a perturbation in ϵWi,

$$u = u^{(0)} + \epsilon Wi\, u^{(1)} + \epsilon^2 Wi^2\, u^{(2)} + O(\epsilon^3 Wi^3), \tag{12a}$$
$$v = v^{(0)} + \epsilon Wi\, v^{(1)} + \epsilon^2 Wi^2\, v^{(2)} + O(\epsilon^3 Wi^3), \tag{12b}$$
$$p = p^{(0)} + \epsilon Wi\, p^{(1)} + \epsilon^2 Wi^2\, p^{(2)} + O(\epsilon^3 Wi^3), \tag{12c}$$
$$\tau_{xx} = \tau_{xx}^{(0)} + \epsilon Wi\, \tau_{xx}^{(1)} + \epsilon^2 Wi^2\, \tau_{xx}^{(2)} + O(\epsilon^3 Wi^3), \tag{12d}$$
$$\tau_{xy} = \tau_{xy}^{(0)} + \epsilon Wi\, \tau_{xy}^{(1)} + \epsilon^2 Wi^2\, \tau_{xy}^{(2)} + O(\epsilon^3 Wi^3), \tag{12e}$$
$$\tau_{yy} = \tau_{yy}^{(0)} + \epsilon Wi\, \tau_{yy}^{(1)} + \epsilon^2 Wi^2\, \tau_{yy}^{(2)} + O(\epsilon^3 Wi^3). \tag{12f}$$

The perturbed variables (Eqs. (12a)–(12f)) are substituted in the thin film Eqs. (3a)–(3f). We obtain explicit equations for the leading order velocity, pressure and stress components

$$u^{(0)} = \frac{1}{2}\frac{dp^{(0)}}{dx}(y^2 - yh) + \left(1 - \frac{y}{h}\right), \tag{13a}$$
$$v^{(0)} = \frac{dh}{dx}\left(2 - 3\frac{h_m}{h}\right)\left(\frac{y^3}{h^3} - \frac{y^2}{h^2}\right) \tag{13b}$$
$$\frac{d}{dx}\left(\frac{1}{12}\frac{dp^{(0)}}{dx}\right) = \frac{dh}{dx}, \tag{13c}$$
$$\tau_{xx}^{(0)} = 0, \tag{13d}$$
$$\tau_{xy}^{(0)} = (1-\beta)\frac{\partial u^{(0)}}{\partial y}, \tag{13e}$$
$$\tau_{yy}^{(0)} = 2(1-\beta)\frac{\partial v^{(0)}}{\partial y}. \tag{13f}$$

The first order velocity, pressure and stress components are

$$u^{(1)} = \frac{1}{2}\frac{dp^{(1)}}{dx}(y^2 - yh) + \frac{1}{h}\frac{dh}{dx}\left(1 - 3\frac{h_m}{h}\right)\left(2 - 3\frac{h_m}{h}\right)(y^2 - yh), \tag{14a}$$

$$\begin{aligned} v^{(1)} = {} & \frac{1}{2}\frac{d^2p^{(1)}}{dx^2}\left(\frac{y^3}{3} - \frac{y^2h}{2}\right) + \frac{1}{2}\frac{dp^{(1)}}{dx}\left(\frac{y^3}{3} - \frac{y^2}{2}\frac{dh}{dx}\right) \\ & \left\{ \frac{1}{h}\frac{d^2h}{dx^2}\left(1 - 3\frac{h_m}{h}\right)\left(2 - 3\frac{h_m}{h}\right) \right. \\ & - \frac{1}{h^2}\left(\frac{dh}{dx}\right)^2\left(1 - 3\frac{h_m}{h}\right) \\ & \left. \times \left(2 - 3\frac{h_m}{h}\right) \right\}\left(\frac{y^3}{3} - \frac{y^2h}{2}\right) \\ & + \frac{9}{h}\frac{dh}{dx}\left\{\left(\frac{h_m}{h^2}\frac{dh}{dx}\right)\left(1 - 2\frac{h_m}{h}\right)\right\}\left(\frac{y^3}{3} - \frac{y^2h}{2}\right) \\ & + \frac{1}{h}\frac{dh}{dx}\left(1 - 3\frac{h_m}{h}\right)\left(2 - 3\frac{h_m}{h}\right)\left(\frac{y^3}{3} - \frac{y^2}{2}\frac{dh}{dx}\right) \end{aligned} \tag{14b}$$

$$\begin{aligned} \frac{d}{dx}\left(\frac{h^3}{12(1-\beta)}\frac{dp^{(1)}}{dx}\right) = {} & \frac{1}{h}\left(\frac{dh}{dx}\right)^2\left(3\frac{h_m^2}{h^2} - \frac{3}{2}\frac{h_m}{h}\right) \\ & + \frac{d^2h}{dx^2}\left(-\frac{1}{3} - \frac{3}{2}\frac{h_m^2}{h^2} + \frac{3}{2}\frac{h_m}{h}\right), \end{aligned} \tag{14c}$$

$$\tau_{xx}^{(1)} = 2\tau_{xy}^{(0)}\frac{\partial u^{(0)}}{\partial y}, \tag{14d}$$

$$\tau_{xy}^{(1)} = -\left(u^{(0)}\frac{\partial \tau_{xy}^{(0)}}{\partial x} + v^{(0)}\frac{\partial \tau_{xy}^{(0)}}{\partial y} - \tau_{yy}^{(0)}\frac{\partial u^{(0)}}{\partial y}\right) + (1-\beta)\frac{\partial u^{(1)}}{\partial y}, \tag{14e}$$

$$\tau_{yy}^{(1)} = -\left(u^{(0)}\frac{\partial \tau_{yy}^{(0)}}{\partial x} + v^{(0)}\frac{\partial \tau_{yy}^{(0)}}{\partial y} - 2\tau_{xy}^{(0)}\frac{\partial v^{(0)}}{\partial x} - 2\tau_{yy}^{(0)}\frac{\partial v^{(0)}}{\partial y}\right) + 2(1-\beta)\frac{\partial v^{(1)}}{\partial y}, \tag{14f}$$

where h_m is the height at the location of maximum pressure and is defined as

$$h_m = \frac{\int_0^1 h^{-2}dx}{\int_0^1 h^{-3}dx}. \tag{15}$$

For further details the reader is referred to Tichy [28] and Li [32]. The boundary conditions for Eq. (14c) are $p^{(1)} = \theta\bar{\tau}_{xx}$ at $x = 0$ and $x = 1$. Note that LIN provides the steady state solution.

2.3.3. Numerical method for GR and LIN

We summarize the numerical method used to solve GR (Eq. (11a)) and LIN (Eq. (14c)). The ordinary differential equation for pressure appearing in both models can be generalized as

$$\frac{d}{dx}\left(\delta\frac{dp}{dx}\right) = f, \tag{16}$$

where δ and f are functions defined in Table 2. We discretize the differential operators via a cell centered finite difference method and use a central difference approximation. The right hand side is either a known function of x or can be discretized via a central difference scheme as well. The discretized equations take the form then

$$W_{i-1}p_{i-1} + C_i p_i + E_{i+1}p_{i+1} = f_i, \tag{17}$$

Table 2
The functions appearing on the left hand side (δ) and right hand side (f) of the GR and the LIN models.

Model	δ	f
GR	$\frac{h^3}{12}$	$\frac{1}{2}\frac{dh}{dx} + \epsilon Wi\,\frac{d}{dx}\left(-\int_0^h \frac{y}{h}\int_0^h \frac{D\tau_{xy}}{Dt}dy'dy + \int_0^h \int_0^y \frac{D\tau_{xy}}{Dt}dy'dy\right)$
LIN	$\frac{h^3}{12(1-\beta)}$	$\frac{1}{h}\left(\frac{dh}{dx}\right)^2\left(3\frac{h_m^2}{h^2} - \frac{3}{2}\frac{h_m}{h}\right) + \frac{d^2h}{dx^2}\left(-\frac{1}{3} - \frac{3}{2}\frac{h_m^2}{h^2} + \frac{3}{2}\frac{h_m}{h}\right)$

where $W_{i-1} = \frac{\delta_i+\delta_{i-1}}{2\Delta x^2}$, $E_{i+1} = \frac{\delta_i+\delta_{i+1}}{2\Delta x^2}$, $C = -(E+W)$ and Δx is the uniform grid spacing. The algebraic system of equations Eq. (17) can be solved via a fast tridiagonal matrix algorithm.

Note that for GR, (i) the shear stress is known when solving for the pressure, thus we can easily evaluate the integrals numerically by trapezoidal rule and (ii) the pressure must be obtained at each time step since the velocity field must be recomputed based on the pressure. On the other hand for LIN, the solution for $p^{(1)}$ is obtained only once for a given profile.

2.4. Direct numerical simulation (DNS)

The most reliable numerical solutions will be obtained from the solution of the Navier–Stokes equations coupled with the Oldroyd-B constitutive equation (Eqs. (1a)–(1c)). However, earlier efforts available in literature demonstrate a strong non-linear instability inherent in this coupling. The LCR was the first robust method that enabled simulations at high Wi [16]. We provide a brief overview of the method.

We introduce the conformation tensor $\mathbf{C}$

$$\boldsymbol{\tau}^* = G(\mathbf{C} - \mathbf{I}), \tag{18}$$

where G is the shear modulus and express the constitutive relation (Eq. (1c)) in terms of $\mathbf{C}$,

$$\frac{\partial \mathbf{C}}{\partial t^*} + (\mathbf{u}^* \cdot \nabla^*)\mathbf{C} - \mathbf{L}^{*T}\mathbf{C} - \mathbf{C}\mathbf{L}^* = \frac{1}{\lambda}(\mathbf{I} - \mathbf{C}). \tag{19}$$

The logarithm of the conformation tensor is defined by

$$\boldsymbol{\psi} = \log(\mathbf{C}). \tag{20}$$

The constitutive equation for $\mathbf{C}$ is recast, via the methodology described by Fattal and Kupferman [16], into a constitutive equation for $\boldsymbol{\psi}$,

$$\frac{\partial \boldsymbol{\psi}}{\partial t^*} + (\mathbf{u}^* \cdot \nabla^*)\boldsymbol{\psi} - \boldsymbol{\sigma}^*\boldsymbol{\psi} + \boldsymbol{\psi}\boldsymbol{\sigma}^* - 2\mathbf{B}^* = \frac{\exp -\boldsymbol{\psi}}{\lambda}(\mathbf{I} - \exp \boldsymbol{\psi}), \tag{21}$$

where $\mathbf{B}^*$ and $\boldsymbol{\sigma}^*$ arise from a decomposition of $\mathbf{L}^*$

$$\mathbf{L}^* = \boldsymbol{\Omega}^* + \mathbf{B}^* + \mathbf{N}^*\boldsymbol{\sigma}^{*-1}. \tag{22}$$

The decomposed tensors $\boldsymbol{\Omega}^*$, $\mathbf{B}^*$ and $\mathbf{N}^*$ are determined by diagonalizing $\mathbf{L}^*$, see Fattal and Kupferman [16] for more details. Therefore, the key is to solve Eq. (21) (i.e. for the logarithm of the conformation tensor) instead of Eq. (19) for the conformation tensor. This logarithmic transformation ensures that the conformation and the stress tensor remain symmetric positive definite.

The DNS in this work is performed via OpenFOAM using LCR which is efficiently implemented by Pimenta and Alves [39]. Although the method is robust, solutions reported in literature at high Wi still break down. There remains a possibility that the breakdown is linked with an intrinsically unstable set of equations at high Wi (i.e. HWNP). However, efforts have been largely directed towards developing special algorithms and numerical schemes that can provide numerical stability. More importantly, a mesh refinement also did not improve the convergence characteristics [40], indicating that there may be a possible limit to this approach [41]. Furthermore, the thin film approximation does not prevent the onset of the HWNP, see Appendix A for details. This points out the need of a simplified model for lubrication type problems able to avoid the computational instability associated to HWNP.

Table 3
The boundary conditions for velocity, pressure and polymer stress applied to the DNS.

Boundary	$x^* = 0$	$x^* = \ell$	$y^* = 0$	$y^* = h^*(x^*)$
p^*	$p^* = 0$	$p^* = 0$	$(\nabla^* p^*)\cdot\mathbf{n} = 0$	$(\nabla^* p^*)\cdot\mathbf{n} = 0$
$\mathbf{u}^*$	$(\nabla^*\mathbf{u}^*)\cdot\mathbf{n} = 0$	$(\nabla\mathbf{u}^*)\cdot\mathbf{n} = 0$	$\mathbf{u}^* = (U, 0)$	$\mathbf{u}^* = (0, 0)$
$\boldsymbol{\tau}^*$	$(\nabla^*\boldsymbol{\tau}^*)\cdot\mathbf{n} = 0$	$(\nabla^*\boldsymbol{\tau}^*)\cdot\mathbf{n} = 0$	$(\nabla^*\boldsymbol{\tau}^*)\cdot\mathbf{n} = 0$	$(\nabla^*\boldsymbol{\tau}^*)\cdot\mathbf{n} = 0$

The boundary conditions for DNS are given in Table 3. In DNS we use only the Newtonian boundary condition for the pressure at $x^* = 0$ and $x^* = \ell$ (i.e. $\theta = 0$). Note that the stress is not directly solved but computed after the intermediate log-transformed variable has been obtained. A zero-gradient condition is assumed for the stresses on all boundaries. A no slip boundary condition is used for the stationary top surface and a fixed velocity is applied at the sliding surface.

2.5. Viscoelastic Reynolds equation (VR)

In this section we introduce (i) the VR model and its assumptions (Section 2.5.1), (ii) discuss the role of the polymer pressure 2.5.2 and (iii) conclude with a brief overview of the numerical procedure used in this study (Section 2.5.3).

2.5.1. Derivation of the VR equation

The need for a new viscoelastic model for lubricants arises by examining the limiting assumptions of GR and LIN (both introduced in Section 2.3). These restrictions do not allow accurate results, especially at large Wi. Hence, we propose a new model able to capture strong viscoelastic effects with better accuracy and imposing no restrictions on the polymer stress. First the model is derived and then the core assumptions are provided. The details of the procedure are provided in Appendix B.

The process starts by integrating twice the x-momentum (Eq. (3b)) along y and utilizing the boundary conditions at the top and the rolling surfaces defined in Section 2.2. After some calculations, we arrive at the following expression for the horizontal velocity field,

$$u(x,y) = \frac{1}{2\beta}\frac{dp}{dx}\left(y^2 - yh\right) + \left(1 - \frac{y}{h}\right) + \frac{1}{\beta}\left(\frac{y}{h}\int_0^h \tau_{xy}dy - \int_0^y \tau_{xy}dy'\right) + \frac{1}{\beta}\left(\frac{y}{h}\int_0^h\int_0^y \frac{\partial\tau_{xx}}{\partial x}dy'dy - \int_0^y\int_0^y \frac{\partial\tau_{xx}}{\partial x}dy'dy\right). \tag{23}$$

Note that the solvent viscosity concentration appears in the denominator which can create a strong singularity for very small values. However, our aim is to decouple the pressure equation from the constitutive relation. Hence the velocity found in Eq. (23) only serves as an intermediate step in deriving VR. The horizontal velocity is substituted into the continuity equation (Eq. (3a)) and the Leibnitz theorem is applied, to obtain the viscoelastic Reynolds equation,

$$\frac{d}{dx}\left(\frac{h^3}{12}\frac{dp}{dx}\right) = \frac{\beta}{2}\frac{dh}{dx} + \frac{d}{dx}\left(\int_0^h \frac{y}{h}\int_0^h\int_0^y \frac{d\tau_{xx}}{dx}dy''dy'dy - \int_0^h\int_0^y\int_0^y \frac{d\tau_{xx}}{dx}dy''dy'dy\right) + \frac{d}{dx}\left(\int_0^h \frac{y}{h}\int_0^h \tau_{xy}dy'dy - \int_0^h\int_0^y \tau_{xy}dy'dy\right). \tag{24}$$

Eq. (24) together with Eq. (23) and the thin film approximation of the Oldroyd-B constitutive relation (Eq. (3d)–(3f)) form a closed system of integral–differential equations. This system involves a non-linear coupling between the unknown quantities and, then, it requires an iterative algorithm to reach a solution. However, the HWNP hinders convergence starting from moderate Wi, even for the thin film approximated system (see Appendix A). To overcome this issue, we assume that the dependence of the velocity field $\mathbf{u}(u, v)$ on the Wiessenberg number is negligible compared to that of the film pressure. In this way we decouple the pressure from the constitutive equation because

the velocity field only depends on a constant leading order pressure (Eq. (13c)).

We need to check the validity of this assumption. Firstly, we define two additional quantities, i.e. the leading and first order volume flow rates as

$$Q^{(0)} = \int_0^h u^{(0)}(x,y)dy \text{ and} \tag{25a}$$

$$Q^{(1)} = \int_0^h u^{(1)}(x,y)dy. \tag{25b}$$

The first order volume flow rate ($Q^{(1)}$) has an analytical expression given by Li et al. [31] which explicitly shows the influence of both the entrance and exit heights of the channel

$$Q^{(1)} = \left\{ \frac{3}{8}h_m^2\left(\frac{1}{h_1^4}-1\right) - \frac{1}{2}h_m\left(\frac{1}{h_1^3}-1\right) + \frac{1}{6}\left(\frac{1}{h_1^2}-1\right)\right\}\int_0^h \frac{1}{h^3}dx, \tag{26}$$

where $h_1 = h(x=1)$ and $h_0 = h(x=0) = 1$. We immediately note that, for channels having $h_1 = 1$, the value of $Q^{(1)}$ is exactly zero. Since the ϵWi-order velocity field $u^{(1)}$ is a quadratic function on y (see Eq. (14a)), it must vanish everywhere to have $Q^{(1)} = 0$. In this case, the horizontal velocity (u) experiences no significant change versus Wi. However, viscoelasticity could affect more significantly the velocity field in asymmetric channels.

We show the strength of the viscoelastic effect in Fig. 2a for the parabolic slider by computing the following quantities.

$$R(Q) = \epsilon Wi Q^{(1)}/Q^{(0)}, \tag{27a}$$

$$R(u) = \max|\epsilon Wi u^{(1)}|/\max|u^{(0)}|, \tag{27b}$$

$$R(v) = \max|\epsilon Wi v^{(1)}|/\max|v^{(0)}|, \tag{27c}$$

$$R(p) = \max|\epsilon Wi p^{(1)}|/\max|p^{(0)}|, \tag{27d}$$

which measure the increase in the maximum of the volume flow rate, velocity field and pressure due to viscoelasticity in LIN. In order to obtain the last quantity (Eq. (27d)), we must solve for the pressure as described in Section 2.3.2. We set $Wi = 100$ to study the case in which presumably the viscoelastic effects are strongest between the configurations analyzed in this paper. In particular we vary the exit location x_e of the parabolic slider represented by Eq. (4) As x_e approaches unity, i.e. the case studied in this work, then (i) the change in the horizontal and vertical velocities becomes smaller and smaller and it can be considered negligible, (ii) on the other hand the change in pressure is very strong and reaches a maximum when $x_e = 1$. Parabolic profiles are used to mimic the contact in roller or journal bearings. For this reason these profiles for practical applications are in general perfectly (or almost) symmetric. While it is true that non-linear effects on the velocity cannot be excluded a priori for slightly asymmetric profiles, we can assume, also for this kind of geometries, that neglecting the effect of viscoelasticity on the velocity and focusing on its effect on the pressure is a reasonable approach.

On the other hand the plane slider is an asymmetric channel with a minimum always occurring at the channel exit, i.e. $h(x=1) = h_1 = \alpha$. In Fig. 2 we show the same quantities of Fig. 2a but as a function of the parameter α. In this case, we observe that viscoelasticity induces a finite change in the quantities for $Wi = 100$. However, note that (i) the change in pressure is always stronger than the change in the velocity, (ii) the change in the horizontal (and as a consequence the flow rate) and vertical velocities is not significant (the maximum values are around 5% and 11%, respectively) and approaches to zero for large α and (iii) the change in pressure also goes to zero as α increases. This implies that the viscoelastic effect for the plane slider is negligible as α is close to $\alpha = 1$. Moreover as α decreases the effect on the pressure is stronger than on the velocity, which strengthens our assumption also for the plane slider. Nevertheless, it is important again to highlight that this observation is an outcome of the thin film approximation combined with a perturbation in ϵWi. There is no guarantee that the order $O(\epsilon^2 Wi^2)$-terms are not significant at large Wi, i.e. when Wi approaches $1/\epsilon$.

2.5.2. Polymer pressure

The pressure equation (Eq. (24)) in the VR model bears similarity to the classical Reynolds equation (Eq. (13c)) for Newtonian lubrication. However, there are three distinct forcing functions appearing on the right-hand-side of Eq. (24). The separation of these terms allows a linear decomposition of the film pressure and, consequently, the load $L = \int_0^1 p(x)dx$. Therefore, the film pressure is expressed as a sum of the contributions due to the solvent and the polymers,

$$p = p_s + p_{xx} + p_{xy}, \tag{28}$$

where p_s is the pressure due to the Newtonian solvent, p_{xx} is the pressure term due to the normal stress τ_{xx} and p_{xy} is the pressure term due to the shear stress τ_{xy}. The total load is decomposed similar to Eq. (28),

$$L = L_s + L_{xx} + L_{xy} = \int_0^1 p_s dx + \int_0^1 p_{xx}dx + \int_0^1 p_{xy}dx, \tag{29}$$

where L_s is the load due to the Newtonian solvent, L_{xx} is the load due to the polymer normal stress and L_{xy} is the load due to the polymer shear stress. Henceforth, for simplicity we will refer to p_{xx} as the normal pressure, p_{xy} as the shear pressure, L_{xx} as the normal load and L_{xy} as the shear load.

For a VR-type model, we assume that the normal and the shear stress are polynomials in y,

$$\tau_{xx} = \sum_{i=1}^{n} T_{xx}^{(i)}(x,t)y^{i-1} \text{ and} \tag{30a}$$

$$\tau_{xy} = \sum_{i=1}^{n+1} T_{xy}^{(i)}(x,t)y^{i-1}. \tag{30b}$$

Substituting Eq. (30) into Eq. (24) and evaluating the integrals we obtain

$$\frac{d}{dx}\left(\frac{h^3}{12}\frac{dp}{dx}\right) = \frac{\beta}{2}\frac{dh}{dx} + \frac{d}{dx}\left(\frac{h^2}{24}\frac{dh}{dx}\sum_{i=1}^{n}\kappa_i\frac{\partial T_{xx}^{(i)}(x,t)}{\partial x} + \frac{h^3}{24}\sum_{i=1}^{n}\omega_i T_{xx}^{(i)}(x,t)\right) + \frac{d}{dx}\left(\frac{h^2}{12}\sum_{i=1}^{n+1}\gamma_i T_{xy}^{(i)}(x,t)\right), \tag{31}$$

where ω_i, κ_i and γ_i are known coefficients arising from the integration.

By examining the RHS of Eq. (31) we find three different terms which control the pressure distribution across the contact. The first term is due to the Newtonian solvent, the second term is due to the normal stress and the last term is due to the shear stress. The exact values of the coefficients of the latter two terms depend on the degree of the polynomial approximations. For instance, if we choose $n = 2$, i.e. a linear polynomial for τ_{xx} and quadratic for τ_{xy}, we can obtain a simple but inaccurate analytical expression. The resulting inaccuracy in the model, owing to a linear approximation for τ_{xx} does not provide definitive conclusions. For this reason we have to choose $n > 2$ and we need to adopt a numerical treatment of Eq. (31).

An explicit equation for p_{xx} and p_{xy} can be obtained by substituting Eq. (28) into Eq. (31). The shear pressure is defined as

$$\frac{d}{dx}\left(\frac{h^3}{12}\frac{dp_{xy}}{dx}\right) = \frac{d}{dx}\left(\frac{h^2}{12}\sum_{i=1}^{n+1}\gamma_i T_{xy}^{(i)}(x,t)\right). \tag{32}$$

Similarly, the normal pressure (p_{xx}) is defined as

$$\frac{d}{dx}\left(\frac{h^3}{12}\frac{dp_{xx}}{dx}\right) = \frac{d}{dx}\left(\frac{h^2}{24}\frac{dh}{dx}\sum_{i=1}^{n}\kappa_i\frac{\partial T_{xx}^{(i)}(x,t)}{\partial x} + \frac{h^3}{24}\sum_{i=1}^{n}\omega_i T_{xx}^{(i)}(x,t)\right). \tag{33}$$

However, note that in the absence of viscoelastic effects, i.e. $Wi = 0$, we can still have a finite concentration of polymers if we choose $\beta < 1$. This means polymers can exhibit a Newtonian stress that must be taken into account by the shear pressure (p_{xy}). Therefore, to examine also the non-Newtonian part, we divide the shear pressure into two components

$$p_{xy} = p_{xy}^{(N)} + p_{xy}^{(NN)}, \tag{34}$$

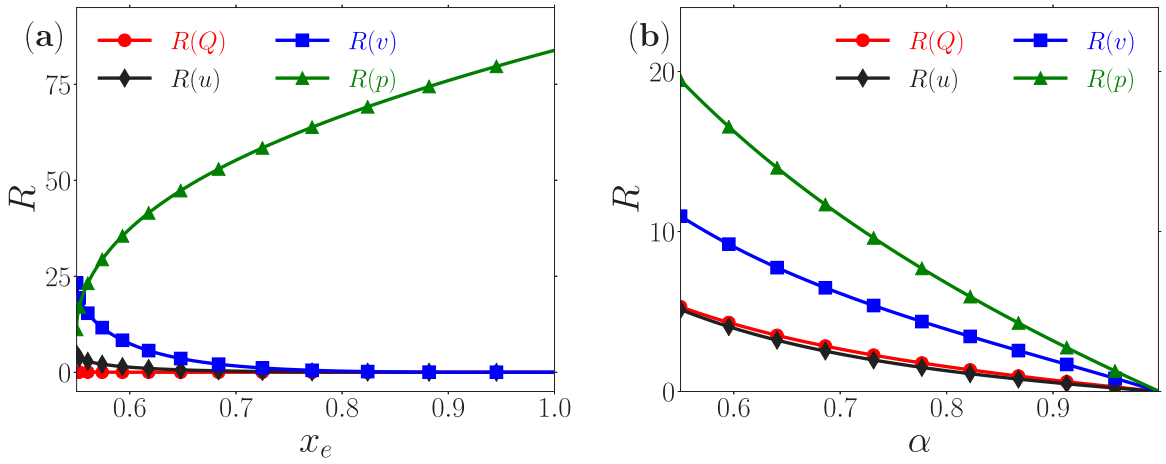

Fig. 2. The percentage change (R) in (red) the volumetric flow rate $R(Q)$, (black) the horizontal velocity $R(u)$, (blue) the vertical velocity $R(v)$ and (green) the pressure $R(p)$ due to viscoelastic effects for the (a) parabolic slider as a function of the channel exit location (x_e) and (b) plane slider as $h(x=1)=\alpha$. The Weissenberg number is set $Wi = 100$ for both figures.

where p^N_{xy} (p^{NN}_{xy}) is the Newtonian (non-Newtonian) shear pressure. Note that the normal pressure has no Newtonian component because the normal strain rate ($\dot{\gamma}_{xx}$) is negligible due to the thin film approximation. The Newtonian portion is simply

$$\frac{d}{dx}\left(\frac{h^3}{12}\frac{dp^{(N)}_{xy}}{dx}\right) = \frac{1-\beta}{2}\frac{dh}{dx}, \tag{35}$$

and the non-Newtonian portion $p^{(NN)}_{12}$ can be retrieved via Eq. (34). Finally, the additional pressure due to viscoelastic effects denoted by p_{ve} is retrieved by summing p_{xx} and $p^{(NN)}_{xy}$

$$p_{ve} = p_{xx} + p^{(NN)}_{xy}. \tag{36}$$

This decomposition will allow us to compare in Section 3.3 the additional pressure due to viscoelasticity in VR to the LIN first order pressure (Eq. (14c)) as an additional step to validate our model at small ϵWi.

2.5.3. Numerical method

The system of the equations of the new viscoelastic model consists of (i) the pressure equation (Eq. (31)) and (ii) the thin film constitutive equations (Eqs. (3d)–(3f)). We prefer to use the purely differential form of VR (Eq. (31)) instead of the integro-differential form (Eq. (24)) since it is simpler to solve. However, both equations are equally valid. Firstly, the polynomial approximations (Eqs. (30)) are used to solve the thin film equations. Based on several numerical trials, we have observed that (i) a cubic polynomial for τ_{xy} (i.e. $n = 3$) is sufficient for small to moderate Wi but (ii) $n = 4$ is a more suitable choice for moderate to large Wi. For this reason we assume that $n = 4$ to get

$$\tau_{xx}(x,y,t) = T^{(I)}_{xx}(x,t) + T^{(II)}_{xx}(x,t)y + T^{(III)}_{xx}(x,t)y^2 + T^{(IV)}_{xx}(x,t)y^3, \tag{37a}$$

$$\tau_{xy}(x,y,t) = T^{(I)}_{xy}(x,t) + T^{(II)}_{xy}(x,t)y + T^{(III)}_{xy}(x,t)y^2 + T^{(IV)}_{xy}(x,t)y^3 + T^{(V)}_{xy}(x,t)y^4 \text{ and} \tag{37b}$$

$$\tau_{yy}(x,y,t) = T^{(I)}_{yy}(x,t) + T^{(II)}_{yy}(x,t)y + T^{(III)}_{yy}(x,t)y^2 + T^{(IV)}_{yy}(x,t)y^3 + T^{(V)}_{yy}(x,t)y^4, \tag{37c}$$

where $T^{(k)}_{ij}(x,t)$ are unknown functions at a given position y across the film. The temporal dependency is explicitly stated because we solve a transient problem.

In order to determine the stress polynomials, we must solve for each of the functions $T^{(k)}_{ij}$, see Appendix C for details. Briefly, we only require the discretization of the temporal ($\partial/\partial t$) and spatial ($\partial/\partial x$) operators appearing in Eqs. (3d)–(3f) since we can calculate analytically the derivative in y of the polynomials (Eqs. (37a)–(37c)). The temporal derivative is discretized using an explicit Euler scheme. The time step Δt was set to $\Delta t = 0.002s$ to have stable simulations. To minimize numerical complexity, we use a finite difference approximation to discretize the spatial derivative with appropriate first-order upwind (downwind) if $u(x) > 0$ ($u(x) < 0$) discretizations for the advective terms. Once we have the solution for the stress polynomials, we simply discretize the LHS of Eq. (31) via a cell-centered finite difference approximation and solve for the pressure, see Section 2.3.3. After several tests, we observed that a number of grid points $N_x = 512$ was suitable for having grid independence also at high values of the Weissenberg number.

To detect when the system reaches the steady state, we use the following criteria for each of the stress components

$$E = \|\tau^{t+\Delta t}_{ij} - \tau^{t}_{ij}\|^2 < 10^{-8}, \tag{38}$$

where E is the Euclidean norm of the stress difference between two consecutive time steps. In the most numerically complex cases (e.g for $Wi = 100$), we needed 3836 time steps to reach the steady state meaning that the required computational time was equal to 43 s.

3. Parabolic slider

In this section, we present the results for the parabolic slider introduced in Section 2.2. The results comprise of (i) the load variation in Section 3.1, (ii) the effect of the solvent concentration in Section 3.2, (iii) a detailed look into the additional pressure due to viscoelasticity in Section 3.3, (iv) a description of the growth of the polymer stress along the channel in Section 3.4 and, finally (v) an analysis about the effect of the boundary conditions in Section 3.5.1.

3.1. Model comparison

In this section we present a comparison between LIN, GR, VR and DNS for the parabolic slider with $\alpha = 0.5$ by using the Newtonian boundary conditions (Eq. (6)). In particular, Fig. 3a shows the total pressure along the lubricated contact for $Wi = 40$. A pressure increase is predicted by all the models except GR. This increase occurs along the first half of the contact showing a significant departure from the Newtonian profile obtained by solving the classical Reynolds equation (RE), see Eq. (13c). Furthermore, a shift in the negative pressure region is also observed enlarging the positive pressure region. Although the apparent difference in pressure may not appear significant at first

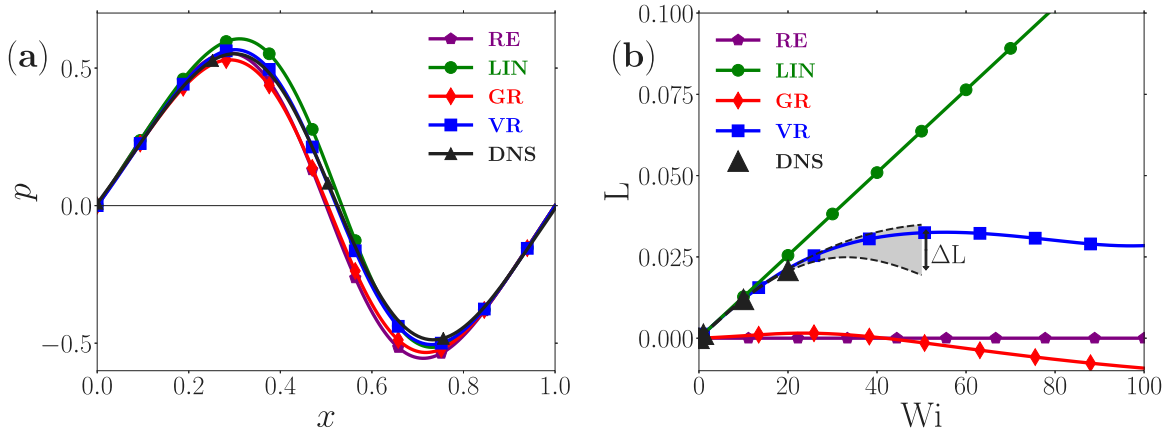

Fig. 3. (a) Pressure profiles for $Wi = 40$ and (b) load versus Wi for the parabolic slider ($\alpha = 0.5$). RE: Newtonian Reynolds equation (Eq. (13c)), LIN: linearized viscoelastic model (Eq. (14c)), GR: generalized Reynolds equation (Eq. (11a)), VR: viscoelastic Reynolds equation with $n = 4$ (Eq. (31)) and DNS: direct numerical simulation (Eqs. (1a)–(1c)). The gray band highlights the uncertainty in the results obtained from DNS.

Table 4
A comparison of computational time taken by different models for the parabolic slider. N/A stands for not applicable, since (i) VR and LIN are one dimensional models and (ii) DNS diverge at $Wi = 100$.

Model	N_x	N_y	Computational time at $Wi = 20$ (s)	Computational time at $Wi = 100$ (s)
LIN	512	N/A	<< 1	<< 1
GR	512	64	24	347
VR	512	N/A	8	43
DNS	512	32	> 3600	N/A

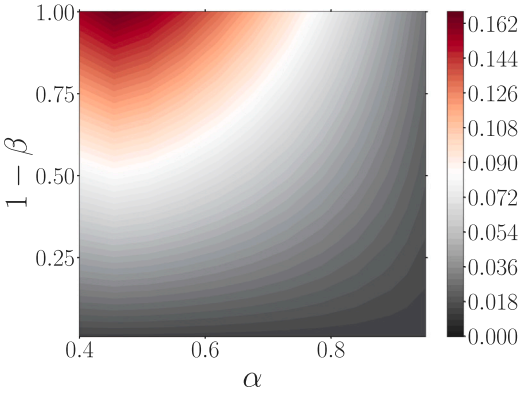

Fig. 4. Total load L contours for in the plane $(1 - \beta, \alpha)$ at $Wi = 60$ for the parabolic slider.

glance, one should note that film pressure in the contact is several MPa in magnitude. Therefore, small shifts and increments represent significant changes in the film pressure from a practical perspective.

Fig. 3b shows the maximum load carrying capacity in function of the Weissenberg number for all the analyzed models. Overall, all models predict an increase in the load carrying capacity. In particular a significant change due to the polymer addition can be observed even at small Wi (but excluding GR). To enable a comparison between the models, we establish the DNS as a benchmark values. However, it should be noted that DNS solutions for fine meshes did not converge beyond $Wi > 20$ due to the HWNP. Convergence was achieved for coarser meshes (until $Wi < 50$) but with some discrepancy in the load value. This failure prevents the successful use of DNS in predicting viscoelastic effects at high Wi. A tolerance region was estimated based on several coarse mesh solutions and is shown by the gray band in Fig. 3b. The tolerance region grows gradually with Wi.

The LIN model predicts a linear increase in the load and performs well for $Wi < 20$ after which it overestimates the load enhancement. Since the departure from DNS occurs around $Wi = 20$, we assume that the range of suitable Wi for LIN is rather small compared to the value suggested by Tichy [28], i.e. $Wi \approxeq 125$. However, from a numerical perspective it is computationally cheap (see Table 4) and suitable for scenarios where Wi is small.

In fact, GR is the least accurate model especially at high Wi. In particular, it greatly deviates from the indicated trend observed for small Wi. Negative loads were obtained for $Wi = 30$ and hence such solutions are considered completely inaccurate. The reason for this failure is that GR neglects the effect of the normal stresses. While this may be true for τ_{yy} under the thin film approximation, it does not hold true for τ_{xx}. This implies that the effect of the normal stress cannot be neglected for any value of Wi. Consequently, the polymer shear stress does not dominate over the normal stresses despite the shear strain rate being several orders of magnitude larger than the axial strain rate. Moreover, GR tends to predict a load decrease below the base Newtonian load indicating an increase in the negative pressure region.

Finally, our proposed VR model compares favorably with the benchmark values. It shows excellent qualitative and quantitative agreement for $Wi \leq 20$ and the solution remains within the estimated tolerance region of the DNS. Therefore, for values of Wi greater than 50, where the benchmark is not available, VR is the best candidate to accurately predict the trend in load. A maximum value for the load is observed close to $Wi \approx 60$, showing that the beneficial effect of the polymers saturates at large Wi. Moreover, VR shows that the variation in load versus Wi is highly non-linear despite a linear constitutive relation. There are several advantages of VR: (i) it captures non-linear trends in the load, (ii) VR does not exhibit that HDNP problem for the values of Wi considered in this work, likely due to the decoupling of the velocity field from the pressure and the stress, (iii) coupling other constitutive relations is trivial, since VR simplifies the thin film constitutive equation via polynomial approximations rather than alter it, (iv) non-uniform meshes can be easily treated since we have shown that fourth degree polynomial approximations are sufficient at moderate to

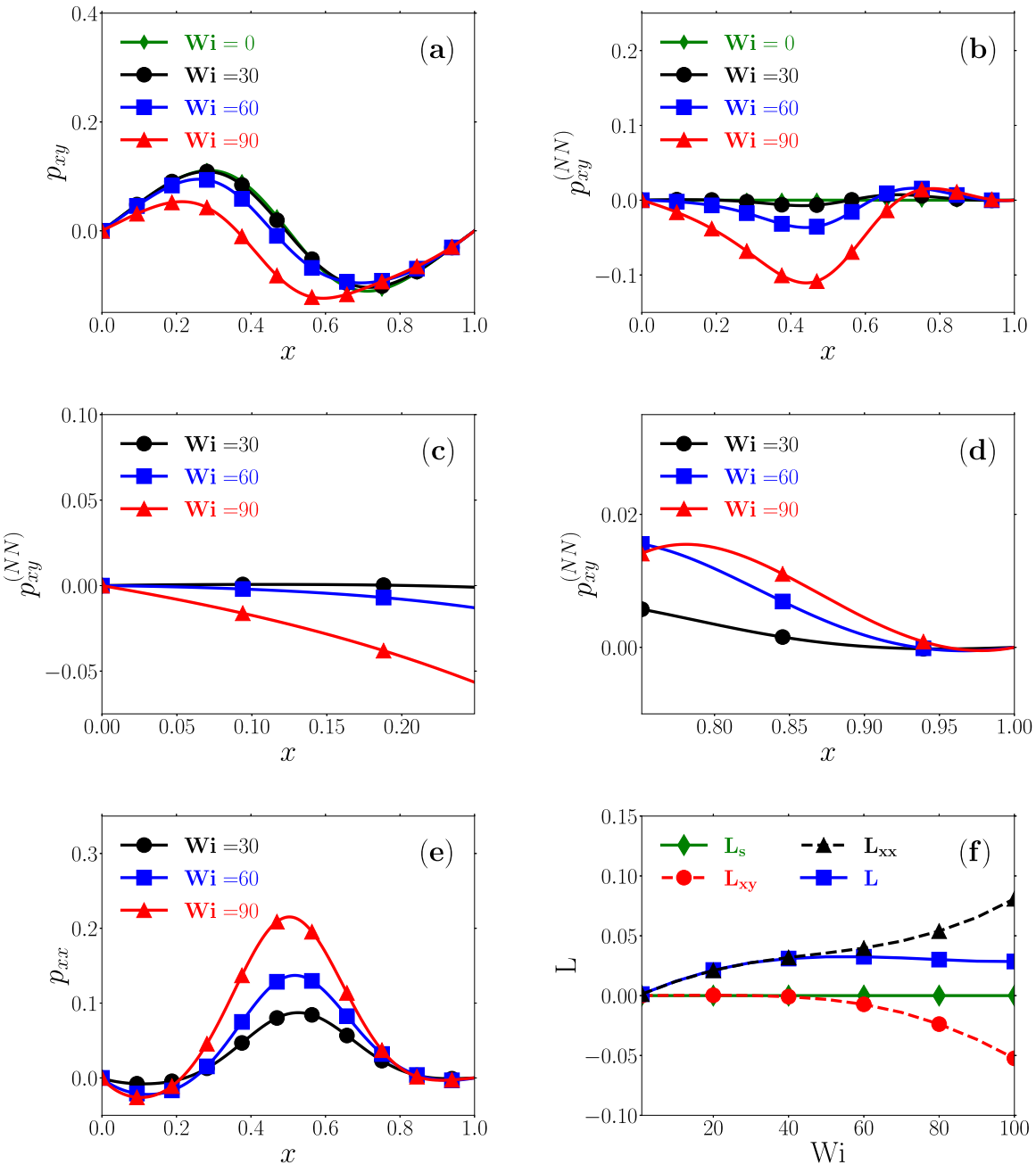

Fig. 5. (a) The shear pressure and (b) the non-Newtonian portion of the shear pressure along the channel for different Wi. (c) Shear pressure distribution close to the inlet and (d) shear pressure distribution close to the outlet regions of the channel for different Wi. (e) The normal pressure p_{xx} along the channel for different Wi. (f) A comparison of the load components versus Wi for the parabolic slider: (i) the Newtonian solvent load (L_s), (ii) the shear load (L_{xy}), (iii) the normal load (L_{xx}) and (iv) the net load L.

high values of Wi and therefore cross-film derivatives of stress can be easily computed, (v) VR is computationally cheap and can therefore be easily extended to simulate complex geometries requiring very fine meshes.

To this regard a comparison of computational time for each model is provided in Table 4. The total time for DNS for $Wi = 20$ is very large despite the efficient implementation of fast numerical algorithms (such as the multigrid method [42]) in OpenFOAM [43]. From a numerical perspective, the GR model requires a two dimensional mesh and a full non-linear coupling of the velocity, pressure and shear stress which is more computationally expensive compared to LIN and VR (see Table 4). Although the simulation time depends strongly on the numerical techniques and algorithms, LIN and VR are faster mainly because they are one-dimensional models. It may be possible to further improve efficiency via more sophisticated techniques but they are not pursued in this study.

3.2. Influence of the solvent concentration and the aspect ratio

The effect of varying β and α for the parabolic slider on the total load is shown in Fig. 4 by using the VR model. Increasing the viscous fraction of polymers $(1-\beta)$ linearly enhances the load. This is expected

because the Oldroyd-B constitutive relation does not factor shear thinning of the polymer. On the other hand as α decreases, the load is enhanced since the velocity gradients along the channel increase.

Note that the VR model can account for $\beta = 0$ which poses numerical problems for DNS, since the momentum equations (Eq. (1b)) lose their elliptical characteristics and become increasingly hyperbolic. This may require advanced numerical techniques for both spatial and temporal discretization [44,45]. On the contrary, VR can assume a fully viscoelastic fluid with $\beta = 0$ without any complications.

3.3. Viscoelastic pressure

In this section, we present the components of the pressure and the load: starting with (i) the shear pressure and the shear load followed by (ii) the normal pressure and the normal load and finally (iii) the additional pressure due to viscoelasticity (see Eq. (36)).

Fig. 5a shows the shear pressure (p_{xy}) distribution for different values of Wi. The shape of the distribution of p_{xy} is not altered significantly but translates towards the negative axis, causing both the maximum and the minimum pressure locations to move closer to the inlet. On the other hand, $p_{xy}^{(NN)}$ does not exhibit the same behavior as Wi increases, see Fig. 5b. We only observe an increase in the absolute value of the maximum and minimum. In Fig. 5c and Fig. 5d, we highlight the inlet and the outlet regions of $p_{xy}^{(NN)}$, respectively. At the inlet, $p_{xy}^{(NN)}$ decreases immediately which indicates that viscoelasticity comes into immediate effect for all the values of Wi. On the contrary, the shear pressure gradually decreases to its Newtonian value regardless of the value of Wi towards the channel outlet. This decrease at the outlet is preceded by a small but noticeable overshoot in $p_{xy}^{(NN)}$. This overshoot moves towards the exit as Wi increases. This strong reaction at the entrance implies that polymers suddenly deform at the contact inlet, while at the exit the polymers will go back smoothly to the undeformed state.

The normal pressure (p_{xx}) can be analyzed similarly to the shear pressure (p_{xy}). Fig. 5e shows the normal pressure for several values of the Weissenberg number. The normal pressure increases with Wi mainly in the central portion of the channel, while it remains unaffected at the outlet. Conversely, at the entrance, a decrease in p_{xx} is observed indicating that viscoelasticity comes into immediate effect similarly to what is observed for p_{xy}. This confirms the hypothesis that the polymers undergo sudden deformation as soon as they enter.

Fig. 5f shows the different components of the load in function of the Weissenberg number. The shear load L_{xy} is slightly damped for low Wi but decreases exponentially beyond $Wi \approx 30$. This is due to the significant distortion in the symmetry of p_{xy} as shown in Fig. 5a. This means that the viscoelastic polymer lowers the effective resistance, since the load is due to the viscous resistance of the film. This decrease in resistance indicates a strong deformation of the entangled polymer chains that stretch and align with the flow [46]. On the other hand, the normal load is always increasing causing the overall load enhancement at small and moderate Wi. The saturation occurring around $Wi = 60$ is given by the opposed effect of L_{xy} and L_{xx}. We are not surprised then by the failure of GR since it does neglect the part of the load due to the normal stress, i.e. the main reason of the increase in load due to viscoelasticity.

Finally, the viscoelastic pressure obtained from LIN and VR are compared in Fig. 6. The discrepancy between the two models begins from $Wi = 10$. Both models capture qualitatively the increasing trend in p_{ve}. Particularly, a good agreement towards the channel exit is observed. This is not surprising since a linearized approximation of the pressure can be sufficient for capturing weak viscoelastic effects as those observed close to the exit. Conversely, the disagreement between the models at the entrance is large, where VR predicts a negative additional pressure as opposed to LIN. Moreover, p_{ve} is symmetric for LIN, whereas the proposed VR model predicts a strong asymmetry with the maximum of p_{ve} moving in the direction of the flow. Therefore, the over prediction of the load by LIN is due to an underestimation of the advective terms. Evidently, another advantage of VR is that it allows to distinguish between the influence of the normal and shear stresses on the pressure.

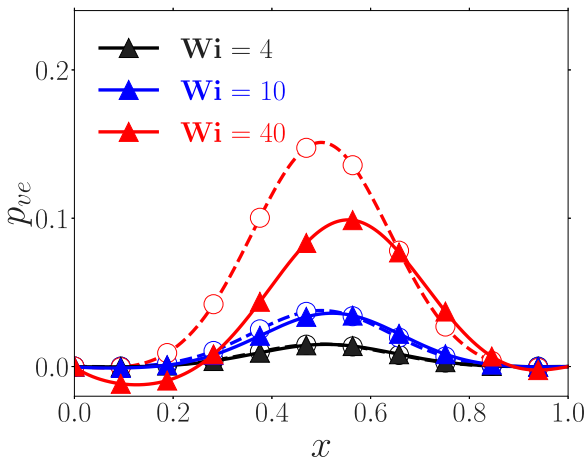

Fig. 6. Distribution of the LIN (dashed line) and VR (solid line) viscoelastic pressure $p_{ve} = \epsilon Wi p^{(1)}$ and $p_{ve} = p_{xx} + p_{xy}^{(NN)}$, respectively for different Wi along the channel.

3.4. Polymer stress

In this section we present the distribution of the shear and the normal stress. In general, the stress gradients are very important since the pressure gradients along the channel strictly depend on them (see Eq. (3b)). Moreover, we can explain the distribution of the stresses in the contact by examining the terms in the constitutive relation (Eqs. (3d)–(3f)). In general, these terms include the advective transport, i.e. the material derivative of the stress and the interaction of the velocity gradient with the other stress components. The latter can be interpreted as source (sink) terms.

Fig. 7a-c (Fig. 7d-f) show the distribution of the polymer shear stress, material derivative and the source (sink) terms appearing in Eq. (3e) for $Wi = 30$ ($Wi = 60$) at $y = h$, $y = h/2$ and $y = 0$, respectively. The primary source term is due to the shear strain rate (green) which is also the Newtonian part of the polymer shear stress. As Wi increases, the total shear stress departs from its initial Newtonian distribution due to the advection and source terms. At the stationary surface, this deviation from the Newtonian distribution is due to the source (blue) terms which eventually subside towards the moving surface. Conversely, at the bottom surface the viscoelastic effect is due to the advection which vanishes moving towards the stationary surface. Furthermore, both these mechanisms strengthen as Wi increases as observed in the discrepancy between the green and black lines (i.e Newtonian and viscoelastic τ_{xy}, respectively), in Fig. 7d–f.

In a similar manner, we examine in Fig. 8 the normal stress that produces the dominant normal load (L_{xx}) and pressure (p_{xx}). In particular, Fig. 8a-c (Fig. 8d-f) illustrate the different terms of the normal stress balance (Eq. (3d)) for $Wi = 30$ ($Wi = 60$) at $y = h$, $y = h/2$ and $y = 0$, respectively. Therefore, viscoelastic polymers also undergo a significant elongation when a large shear strain rate is applied. Furthermore, the source term remains dominant across the contact height and is strongest (weakest) at the stationary (moving) boundary indicative of stress accumulation (dissipation). This growth (decay) is due to the presence of weak (strong) advection at the top (bottom) surface. Finally, as viscoelastic effects increase, all the terms increase in magnitude and the overall normal stress increases which is observed by comparing Fig. 8a–c to Fig. 8d–f.

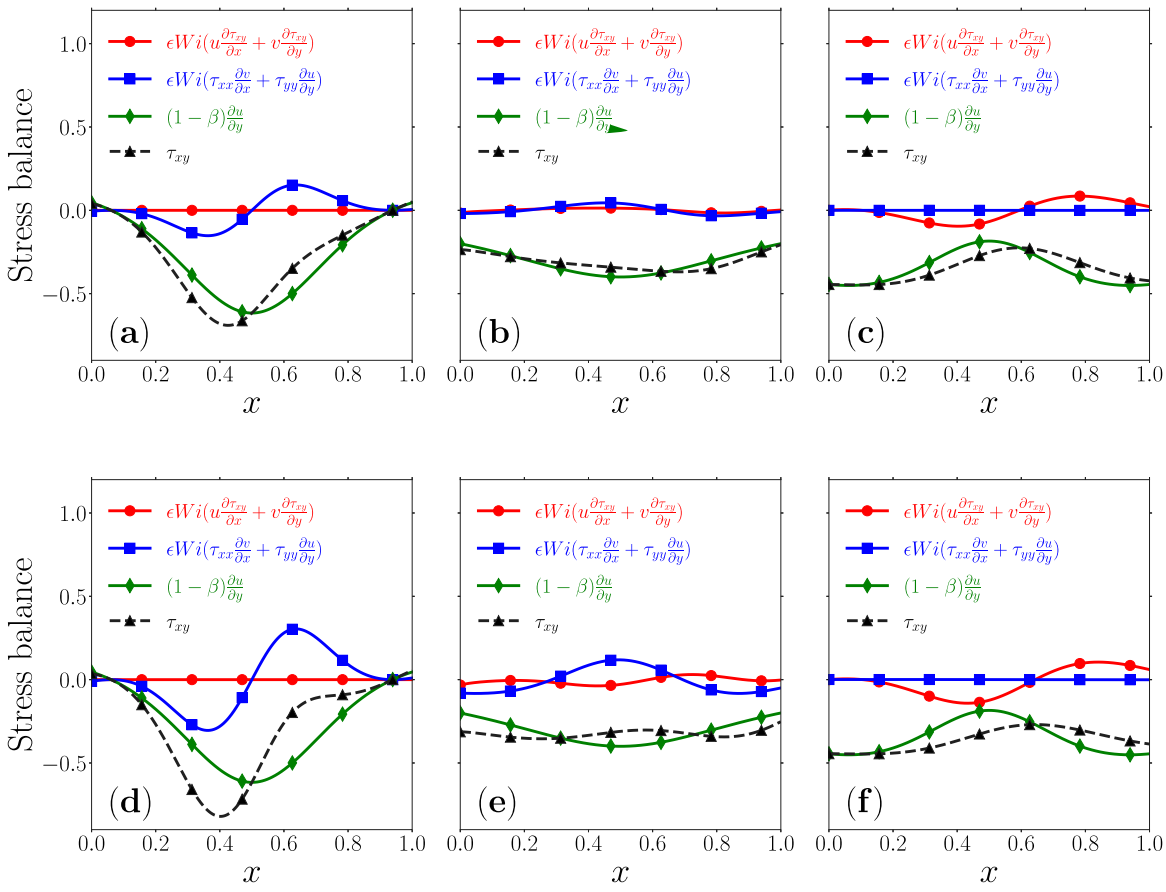

Fig. 7. Spatial distribution of the shear stress (black), the material derivative (red), source terms (blue) and shear strain rate (green) in the shear stress balance (Eq. (3e)) at $Wi = 30$ (a) $y = h$, (b) $y = h/2$, (c) $y = 0$ and $Wi = 60$ (d) $y = h$, (e) $y = h/2$, (f) $y = 0$ for the parabolic slider.

3.5. Influence of the boundary conditions

In this section we show the influence of the boundary conditions introduced in Section 2.2. In particular the limiting case of $\theta = 1$, i.e. the normal stress boundary condition, is discussed in Section 3.5.1. Afterwards, in Section 3.5.2, we take into consideration the influence of the parameter θ.

3.5.1. Normal stress boundary condition

In this section we show the influence of the normal stress boundary condition (Eq. (7)) on the load carrying capacity for the parabolic slider. Fig. 9a shows the pressure distribution along the channel at $Wi = 40$. The finite normal stress at the inlet creates a net vertical shift in the total pressure profile which is captured by both LIN and VR. As a result of this shift, we find that the bulk pressure has increased and the region of negative pressure has reduced. Thus, we observe a large overall increase in the pressure. In Fig. 9b we compare the load variation versus Wi for different models. An increasing trend similar to Fig. 3b is observed. However the trend seems more linear for these boundary conditions and, thus, the region of agreement between LIN and VR dramatically increases.

However, this increase is mainly due to a large finite pressure at the boundaries. We can divide the load in two components: (i) the load due to pressure variation at the boundaries $L_b = \frac{p(0)+p(1)}{2}$ and (ii) the load due the pressure variation along the channel $L_c = L - L_b$. In Fig. 9c we show the evolution of L_b and L_c compared to L. The linear increase of the pressure at the boundaries is greater than its non-linear variation in the middle of channel causing the almost linear behavior of the total load L. However it should be observed that the evolution of L_c follows closely the evolution of the load for the Newtonian boundary conditions (see Fig. 3b). Furthermore, the increase in load due to L_b is several times larger than L_c for moderate to large Wi.

3.5.2. Influence of θ

Fig. 10 shows how the load dependence on θ for $Wi = 40$. While L_b varies linearly with θ, L_c is almost unaffected by this parameter. The sum of the two components L is then obviously linear as L_b. Similar trends were obtained for different values of Wi and α. The linear trend is not surprising since we defined that the pressure at the boundaries varies linearly with θ (see Eq. (8)). While this result cannot clarify which value is the best choice for θ to have a quantitatively accurate value for the load, we can conclude that analyzing the limiting cases is still worthwhile since the most appropriate boundary condition could be a "mix" of the Newtonian and the normal stress boundary conditions.

4. Plane slider

In this section we analyze the plane slider described in Section 2.2 (see Fig. 1a). The main goal is to check the quality of our new approach for a different geometry and examine the effect of the surface geometry on the polymer pressure. In section we start the analysis 4.1 with applying the Newtonian boundary conditions. Afterwards, we introduce in Section 4.2 the normal stress boundary conditions. In this section, we also present a comparison with results available for the plane slider using a second order fluid model [38], which is a constitutive relation valid only at small ϵWi [47]. Finally, the influence of the parameter θ is analyzed in Section 4.3.

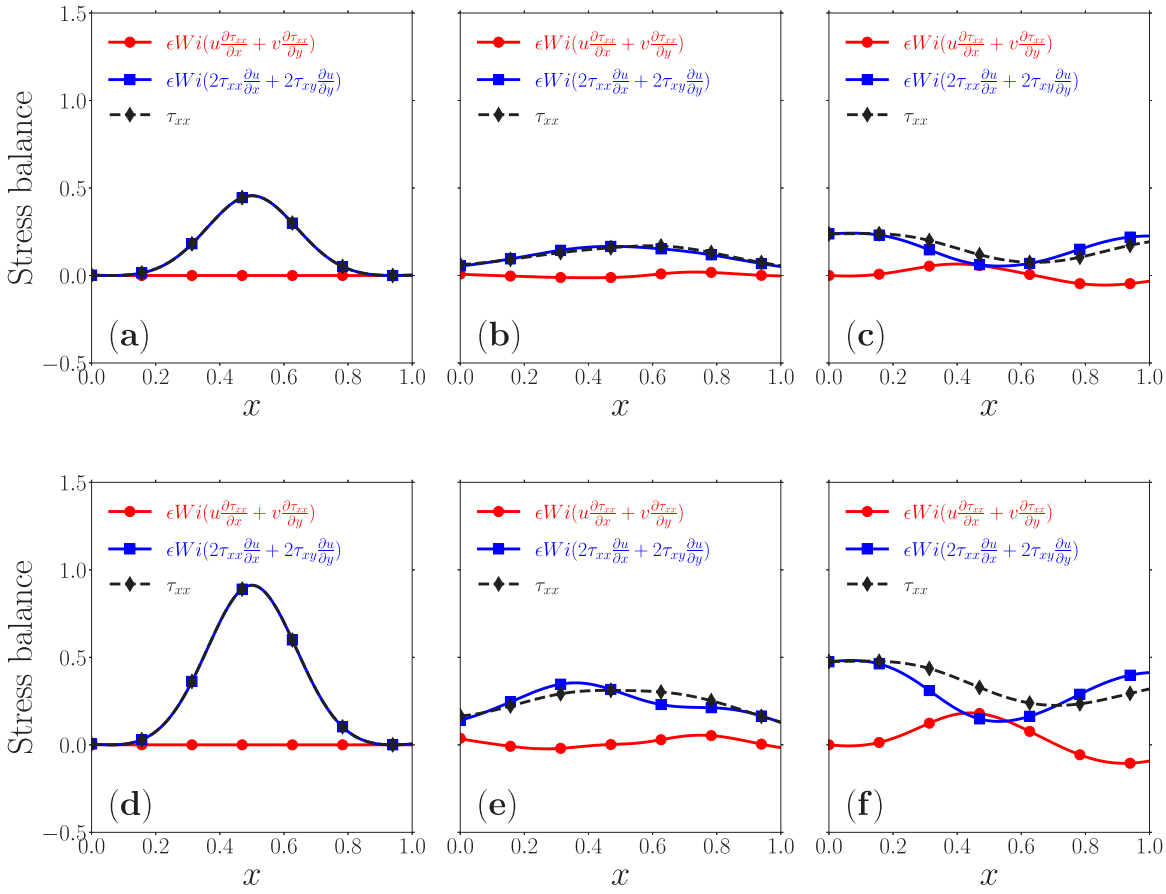

Fig. 8. Spatial distribution of the normal stress (black), the material derivative (red) and source terms (blue) in the normal stress balance (Eq. (3d)) at $Wi = 30$ (a) $y = h$, (b) $y = h/2$, (c) $y = 0$ and $Wi = 60$ (d) $y = h$, (e) $y = h/2$, (f) $y = 0$ for the parabolic slider.

4.1. Newtonian boundary condition

In Fig. 11a the pressure distribution along the contact is reported for RE, LIN and VR ($Wi = 40$) by using the Newtonian boundary condition (Eq. (6)). We compare only these three models because we have seen that for the parabolic slider (Section 3) GR cannot capture the load accurately, whereas DNS does not converge for moderate to high Wi. Both LIN and VR predict a decrease in the film pressure, which rises to a maximum and decays sharply towards the exit. Note that the maximum pressure point does not shift, instead it decreases gradually with Wi. The observed pressure decrease occurs mainly along the center of the channel, close to the peak pressure. Although, the discrepancy between the pressure distribution is graphically small, the prevailing film pressure is several MPa in magnitude. Hence, this small difference is very important from a practical perspective.

Fig. 11b shows the load variation for the plane slider for $\alpha = 0.6$. The plane slider experiences a gradual decrease in the load carrying capacity. Furthermore, LIN provides accurate quantitative estimates for load at small Wi but fails to capture the non-linear trend observed at high Wi.

Fig. 12a illustrates the shear pressure for different Wi for the plane slider. In contrast to the parabolic slider, p_{xy} gradually increases due to a constant increase in $p_{xy}^{(NN)}$ as viscoelastic effects increase, see Fig. 12b. Therefore, the polymers enhance the shear resistance of the film. The increase in pressure with Wi is gradual as opposed to the parabolic slider (Fig. 5) where a strong variation in the shear pressure is observed beyond $Wi \approx 30$. In Fig. 12c the distribution of the normal pressure (p_{xx}) is shown for several values of Wi along the contact. Contrary to the parabolic slider (Section 3), the normal pressure is negative along the channel and causes a reduction of the total pressure. Therefore, as the polymer stretches we find that it acts to reduce the films resistance for the linear surface.

In Fig. 12d we report the solvent load (L_s), the shear load (L_{xy}) and the normal load (L_{xx}). The solvent load is constant because it is purely Newtonian. We find that the shear load rises gradually with Wi exhibiting a weak response to the polymer addition. Therefore, we note that the load is always decreasing, at least within the range of examined Weissenberg numbers. On the other hand, the normal load is negative and larger in magnitude, due to which the total load diminish.

4.2. Normal stress boundary condition

In this section we examine the normal stress boundary conditions given by Eq. (7). We first start with a comparison of VR and LIN with those available in literature for the second order fluid [38] as further validation of our proposed approach. The second order fluid is defined as

$$\boldsymbol{\tau}^* = \eta \mathbf{A}^* - \eta\lambda \mathbf{B}^* + \eta\lambda_{00}\mathbf{A}^{*2}, \tag{39}$$

where $\mathbf{A}^*$ ($\mathbf{B}^*$) is the first (second) Rivlin–Ericksen tensor and λ_{00} is the polymer retardation time. The tensors are expressed in terms of the velocity gradient tensor $\mathbf{L}^*$ as

$$\mathbf{A}^* = \mathbf{L}^* + \mathbf{L}^{*T}, \tag{40a}$$

$$\mathbf{B}^* = \frac{D\mathbf{A}^*}{Dt^*} - \mathbf{L}^*\mathbf{A}^* - \mathbf{A}^*\mathbf{L}^{*T}. \tag{40b}$$

The second order model approximates the polymer stress as a function of the Newtonian strain rate. Therefore, it is a linearization of the stress tensor and can lead to error as the Wi number grows. However, the approach presented in this work uses the Oldroyd-B model which

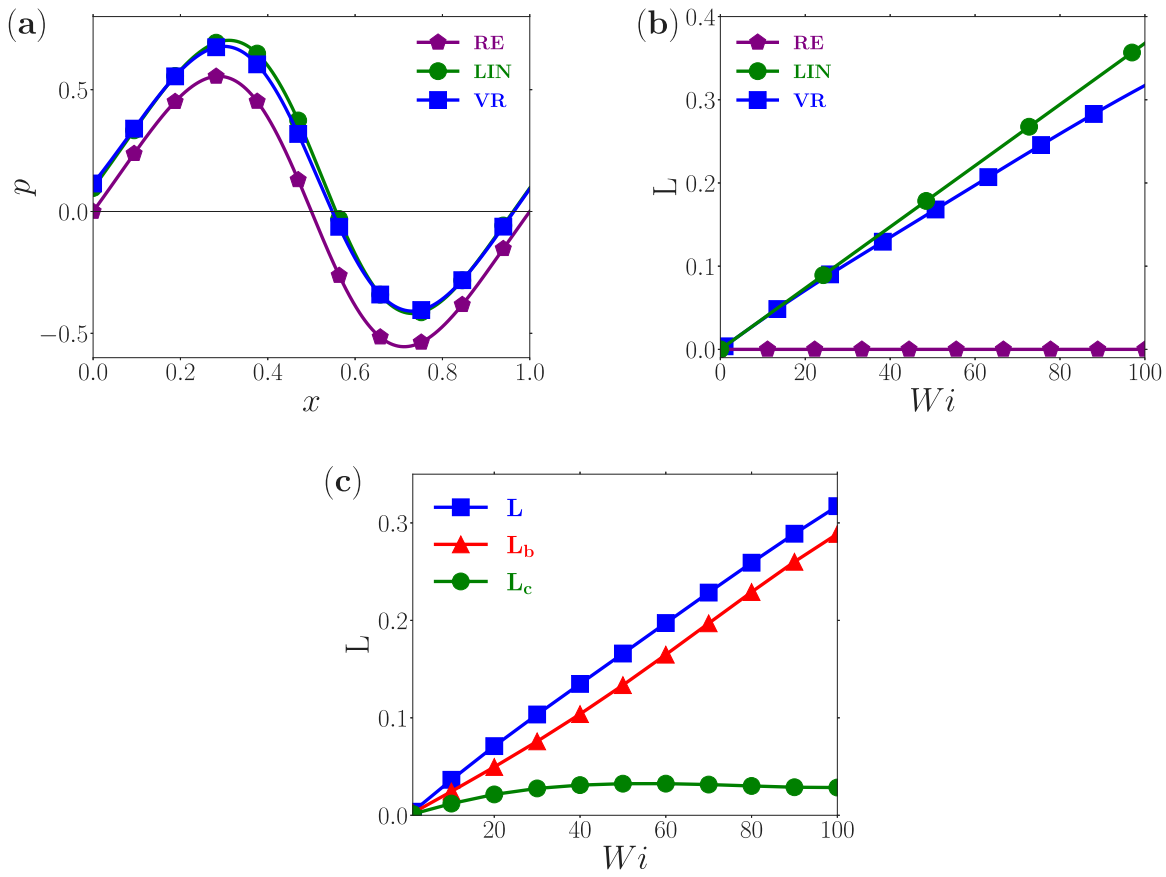

Fig. 9. (a) Pressure along the channel at $Wi = 40$, (b) load versus Wi for different models and (c) the load due to variation of the pressure (i) at the (L_b) and along the channel (L_c) for the parabolic slider. In all these figures the normal stress boundary conditions are applied.

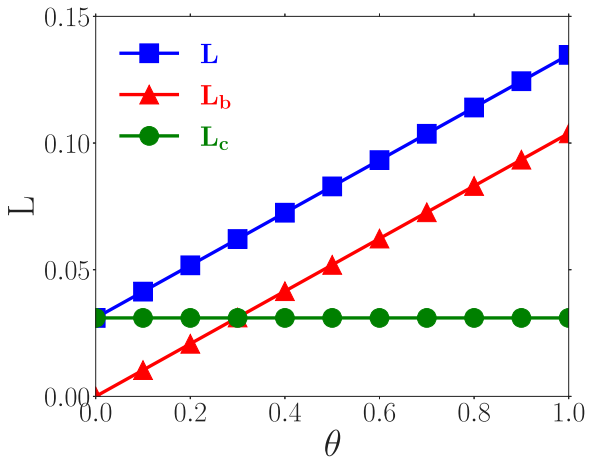

Fig. 10. Load due to the pressure variation at (i) the boundaries (L_b), (ii) along the channel (L_c) and (iii) their sum (L) versus θ for the parabolic slider at $Wi = 40$.

does not restrict the polymer stress in any manner. For further details regarding the second order fluids, the reader is referred to Phan-Thien and Mai-Duy [48].

Fig. 13a (Fig. 13b) compares the pressure distribution along the channel obtained by LIN (dotted green lines), VR (continuous blue lines) and second order fluid (dashed red lines) for different Wi, at $\alpha = 0.8$ (different α, at $Wi = 50$) and for $\beta = 0$. Note that the second order fluid's pressure distribution are extracted from [38]. We find (i) that the pressure increases with Wi and α and (ii) VR and LIN can retrieve the solution given by the second order fluid model. Since the plane slider at $\alpha = 0.8$ is not steep, we observe in general only a small change in the pressure due to the polymer addition. At $\alpha = 0.6$ we begin to observe a difference between the models towards the outlet of the slider. In general, for large values of α a linearized approach seems sufficient for the plane slider with normal stress boundary conditions since it is not sensitive to the non-linear effects due to viscoelasticity.

Fig. 13c compares the load versus Wi for $\alpha = 0.6$ showing a net increase in the load for all the models. This is due to a positive pressure at the inlet and outlet of the channel. Again VR and LIN show a similar behavior since viscoelastic effects are weak for the plane slider with normal stress boundary conditions.

Fig. 13d compares the contribution of the load due to the variation of the pressure (i) at the boundaries L_b and (ii) along the channel L_c calculated with VR. We find an almost linear change in L_b which hides the non-linear variation along the channel. Thus, the large increase of the pressure at the boundaries suppresses the comparatively small decrease along the channel. Similar to the parabolic slider, we find a large difference between L_b and L_c. In fact, from Fig. 13b, we find that the polymers significantly enhance the pressure (and consequently the load) also for a flat slider. In particular for this parallel bearing, this large increase in the load due to L_b may not be physical [36].

4.3. Influence of θ

Fig. 14 shows the influence of θ on (i) the total load L, (ii) the load due to the pressure variation at the boundary L_b and (iii) the

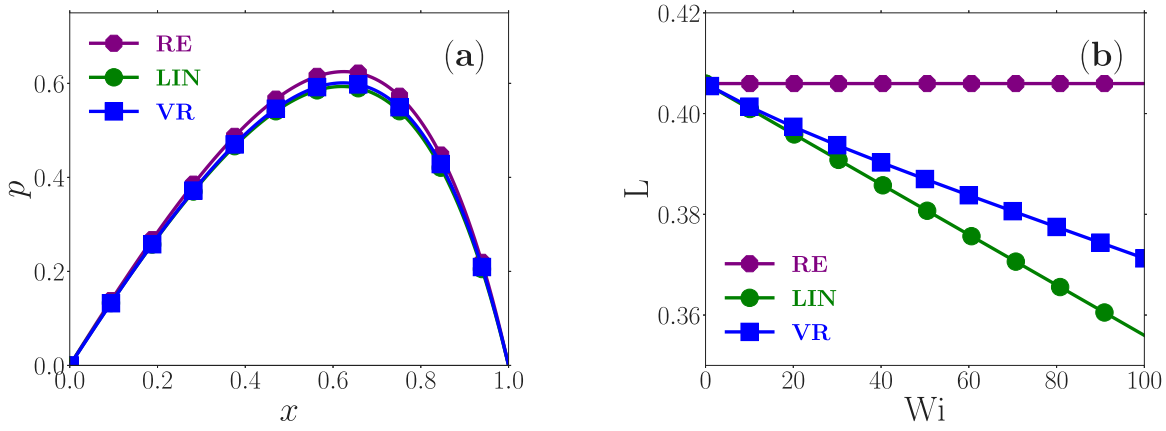

Fig. 11. (a) Pressure distribution for different models along the channel (Fig. 1a) for $Wi = 40$ and (b) the load L versus Wi for the plane slider.

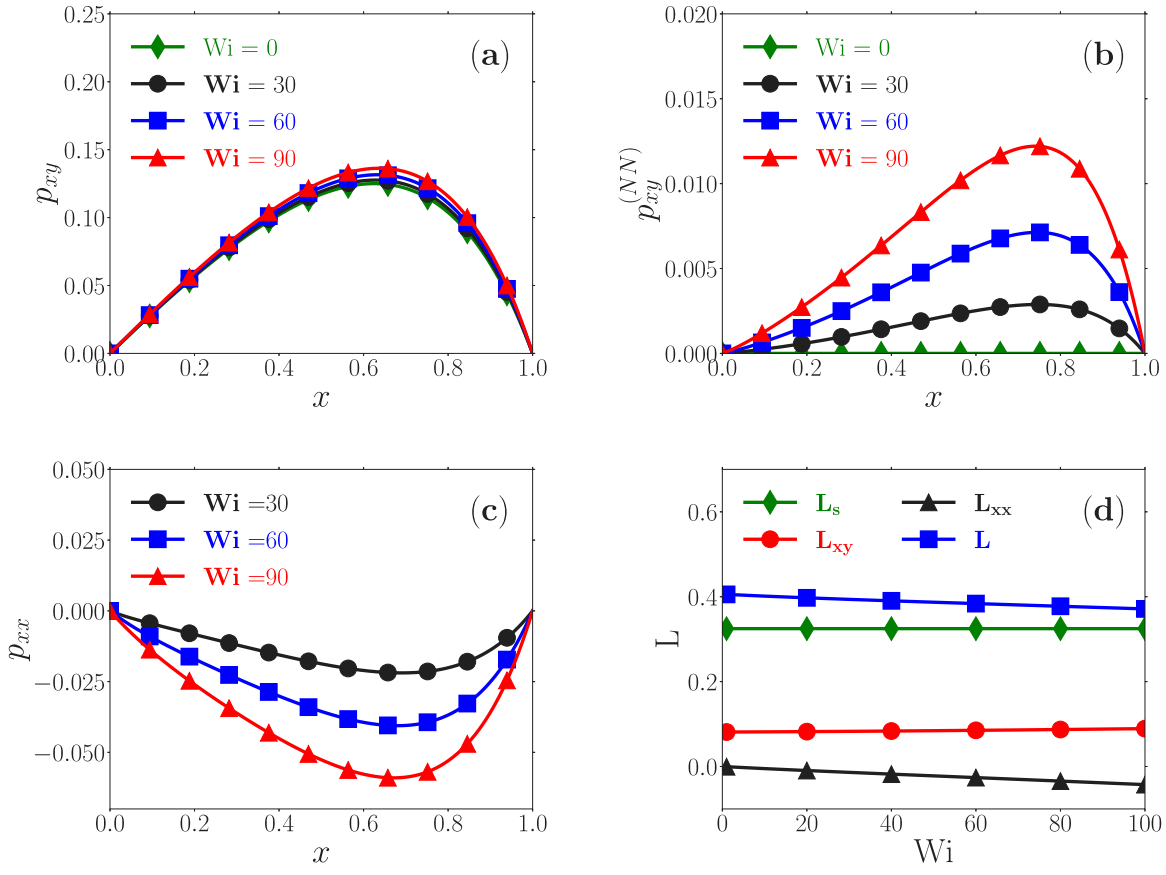

Fig. 12. (a) Polymer shear pressure (i.e. $p_{xy} = p_{xy}^{(N)} + p_{xy}^{(NN)}$), (b) the non-Newtonian portion of the shear pressure ($p_{xy}^{(NN)}$), (c) the pressure due to the normal stress (p_{xx}) for different values of Wi along the plane slider. (d) A comparison of the load components versus Wi: (i) the Newtonian solvent load (L_s), (ii) the shear load (L_{xy}), (iii) the normal load (L_{xx}) and (iv) the net load for the plane slider.

load due to the pressure variation along the channel L_c. We find, again unsurprisingly, that the load varies linearly since the boundary conditions are a linear function of θ (see Eq. (8)). L_b is much more affected by variations in θ than L_c, since its value directly depends on the boundary conditions. Despite these results do not shed light on the validity of the boundary conditions, we conclude that it is still worthwhile to analyze the two limiting cases since we can understand more clearly the behavior of the two loads, L_b and L_c, since they are dominant at $\theta = 1$ and $\theta = 0$, respectively.

5. Discussions about the surface geometry

We observed in the previous two sections that, overall, the results for the plane slider are in stark contrast to the parabolic slider, indicating a strong dependence of the viscoelastic pressure components on the contact shape. Particularly, in Section 3.1 (Section 4.1) we obtained an increase (decrease) in the load carrying capacity due to the addition of the polymers to the lubricant with using the Newtonian boundary conditions. A similar behavior was found in the evolution of L_c, see

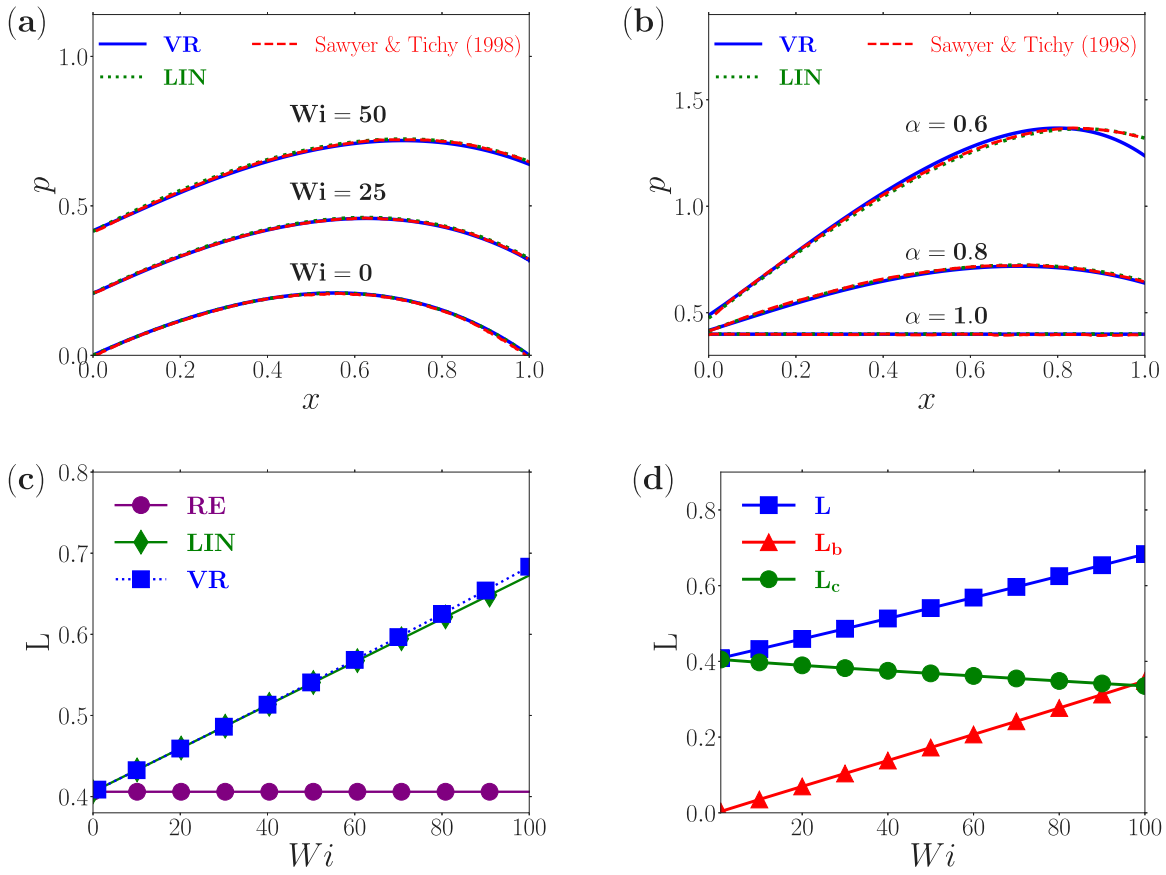

Fig. 13. The variation of the pressure along the channel for different models and $\beta = 0$ as (a) the Wi number is varied for $\alpha = 0.8$, (b) α is varied for $Wi = 50$ where the red curves represent the second order fluid results [38]. (c) The load versus Wi for different models and $\alpha = 0.6$, and (d) comparison of the load calculated with VR due to the variation of the (i) pressure boundary values (L_b) and (ii) pressure along the channel (L_c) for $\alpha = 0.6$. In all these figures the normal stress boundary conditions are applied.

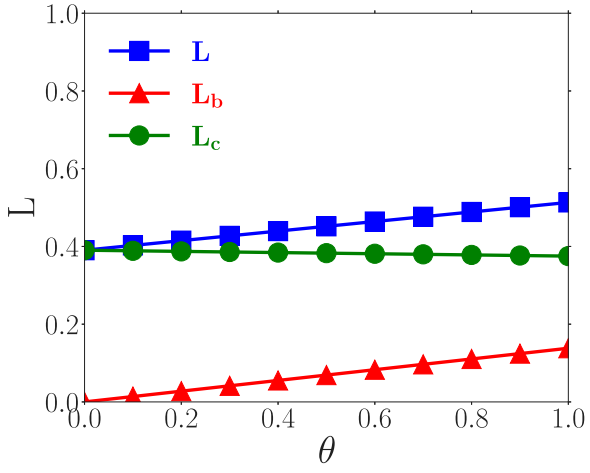

Fig. 14. Load due to the pressure variation at (i) the boundaries (L_b), (ii) along the channel (L_c) and their sum (L) versus θ for the plane slider at $Wi = 40$.

Sections 4.2 and 3.5.1. In the present section we explain this difference in the viscoelastic response.

While VR is indeed accurate for moderate to high Wi, however it does not provide explicit expressions for the pressure as a function of the surface profile and its derivatives. Therefore, we opt to examine the forcing terms appearing in the LIN model (i.e. the RHS in Eq. (14c)) since it has a qualitative behavior at small Wi similar to VR. We assign the forcing functions F_1 and F_2 based on the RHS of Eq. (14c) as

$$F_1 = \frac{1}{h}\left(\frac{dh}{dx}\right)^2\left(3\frac{h_m^2}{h^2} - \frac{3}{2}\frac{h_m}{h}\right), \quad \text{and} \tag{41a}$$

$$F_2 = \frac{d^2h}{dx^2}\left(-\frac{1}{3} + \frac{3}{2}\frac{h_m^2}{h^2} - \frac{3}{2}\frac{h_m}{h}\right). \tag{41b}$$

The forcing terms mainly influence the second derivative of $p^{(1)}$ which determines how rapidly the pressure gradient will rise or drop. F_1 (F_2) depends mainly on the first (second) derivative of the surface shape $h(x)$.

In Fig. 15a we show the forcing term F_1, while $F_2 = 0$ for the plane slider. Note that F_1 is always positive since $h < 2h_m$ for all x. Furthermore, the (i) first order pressure distribution and its (ii) first and (iii) second derivatives are illustrated in Fig. 15b for the plane slider. Since $F_1 > 0$, the initially negative pressure gradient rises gradually until the channel exit. Hence, $p^{(1)}$ decreases to a minimum within the channel due to the negative pressure gradient and recovers to the boundary value (i.e. $p^{(1)} = 0$) as the pressure gradient reverses. This change in sign occurs far from the inlet which prevents $p^{(1)}$ from acquiring a positive value even when the pressure gradient is positive.

Similarly, we show in Fig. 16 the distribution of (a) the forcing terms and (b) the first order pressure and its derivatives for the parabolic slider. Note that F_1 is again always positive since $h < 2h_m$ but this time is strong enough to make the first order pressure gradient positive immediately after the inlet. However, F_2 becomes significantly negative and exceeds the positive F_1 causing the decrease of the first order pressure gradient. This forces $p^{(1)}$ to reduce and arrive at its boundary value at the exit (i.e. $p^{(1)} = 0$). Hence, the second derivative

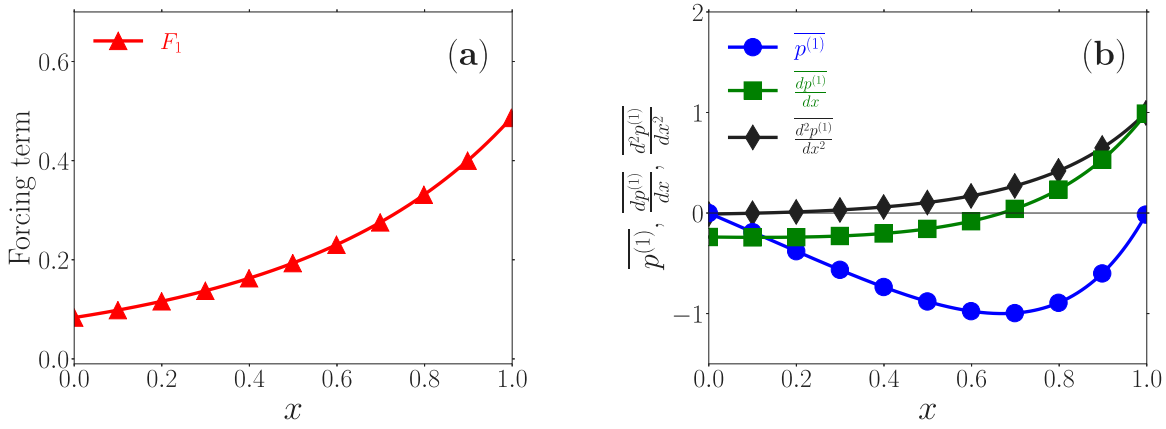

Fig. 15. Distribution of (a) the forcing term (F_1) and (b) the normalized first order pressure $\overline{p^{(1)}} = p^{(1)}/\max|p^{(1)}|$, its first $\overline{\frac{dp^{(1)}}{dx}} = \frac{dp^{(1)}}{dx}/\max\left(\left|\frac{dp^{(1)}}{dx}\right|\right)$ and second derivative of the first order pressure $\overline{\frac{d^2p^{(1)}}{dx^2}} = \frac{d^2p^{(1)}}{dx^2}/\max\left(\left|\frac{d^2p^{(1)}}{dx^2}\right|\right)$ for the plane slider shown in Fig. 1b. Note that the first order pressure and its derivatives are normalized by their own maximum value.

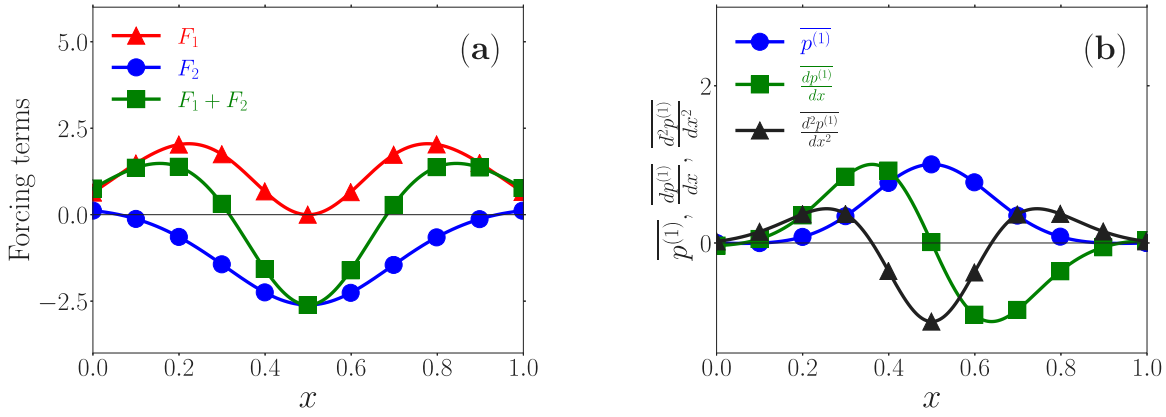

Fig. 16. Distribution of (a) the forcing terms (F_1, F_2 and ($F_1 + F_2$)) and (b) the first order pressure $\overline{p^{(1)}} = p^{(1)}/\max|p^{(1)}|$, its first $\overline{\frac{dp^{(1)}}{dx}} = \frac{dp^{(1)}}{dx}/\max\left(\left|\frac{dp^{(1)}}{dx}\right|\right)$ and second derivative $\overline{\frac{d^2p^{(1)}}{dx^2}} = \frac{d^2p^{(1)}}{dx^2}/\max\left(\left|\frac{d^2p^{(1)}}{dx^2}\right|\right)$ along the parabolic slider shown in Fig. 1a. Note that the first order pressure and its derivatives are normalized by their own maximum value.

of the surface opposes the surface slope diminishing the rate at which the pressure gradient increases (i.e. reducing the second derivative of the pressure) along the channel.

In conclusion, the surface slope in either case enhances the rate at which the first order pressure accumulates within the channel. However, for the same channel length, the plane slider has a constant and comparatively small slope, close to the inlet, which prevents the rapid growth of the pressure gradient which is observed for the parabolic slider. Therefore, we observe a rapid rise of the first order pressure in the parabolic slider which is eventually offset by the negative effect due to F_2, i.e. higher surface gradients (d^2h/dx^2).

6. Conclusions

In this paper a viscoelastic Reynolds (VR) equation is introduced showing a good quantitative and qualitative agreement with the DNS at low and moderate Weissenberg numbers. The good accuracy of VR is reached by (i) preserving the non-linear nature in Wi of the thin film approximated polymer constitutive equations (in contrast to the linearized models) and (ii) by keeping all the terms in such equations (differently from the other non-linearized models found in literature). We do not incur the HWNP in VR since we decouple the velocity field from the pressure equation and the polymer stress. A further advantage of VR is that, by using this decomposition, we can also find the additional viscoelastic pressure and load, similarly to LIN. In addition, we can decompose the load due to the polymers into (i) a shear (i.e. due to the shear stress) and (ii) normal (i.e. due to the normal stress) component.

Furthermore, we have clearly shown the limits of (i) DNS and (ii) the most common models available in literature based on lubrication theory, such as GR and LIN, in describing viscoelastic lubricants. Although modeling viscoelastic effects in lubricated contacts via DNS is the most accurate method, the onset of HWNP occurs at a very small values of Wi. For this reason either convergence cannot be obtained or the solution's accuracy is questionable. We can use LCR to attain solutions for relatively small Wi but eventually HWNP emerges again making impossible to achieve accurate results for $Wi > 20$. On the other hand, simplified models, such as GR, cannot predict the load accurately due to inherently restrictive assumptions regarding the normal stress. LIN can predict the load for small values of Wi but fails to capture the strong non-linear trend at high Wi. We show by comparison with DNS and VR that this limit on LIN is close to $Wi \approx 15$ for the parabolic slider analyzed in this study when using Newtonian boundary conditions.

In this work, we show that viscoelasticity has a strong influence on the lubricant film pressure even at small values of the Weissenberg number. By comparing two different geometries (i.e. a parabolic vs plane slider) we observed that, as Wi increases, the load due the pressure variation along the channel is noticeably enhanced for the quadratic surface, while it reduces for the linear surface. This difference between the parabolic and plane slider is due to the presence (or absence) of higher surface derivatives. The first (second) derivative of the surface enhances (reduces) the rate at which pressure gradients

change along the channel. Since the parabolic slider allows for larger surface slopes close the inlet, the viscoelastic pressure rises rapidly in this region.

In this paper we have also examined the effect of both the solvent concentration and the aspect ratio. Their influence would be more interesting in a constitutive model that is non-linear in the polymer stress, such as FENE-P or PTT . Moreover, polymers are added to lubricants to offset the decrease in viscosity as temperature increases [49]. Therefore, the influence of temperature on the load carrying capacity for a viscoelastic lubricant can be studied more accurately with VR. Additional effects such as piezoviscosity [50] or compressibility [51] can also interact with viscoelasticity. The combination of these effects will enhance the non-linear nature of the equations and might prove to be too expensive for DNS. Furthermore, novel methods to improve load carrying capacity such as surface texturing in the presence of polymer enhanced lubricants [52] may require very fine meshes and accurate results at high Wi. For this reason the proposed VR offers a simplified approach to couple viscoelastic, geometric and rheological effects without increasing the numerical complexity.

Finally, we observed that the total increase in the load for the parabolic slider was due to a shift in the negative pressure region, and a net increase in the pressure. This shift may be of vital importance if the pressure falls below the saturation pressure allowing the formation of a cavitation bubble as usual in bearings [53,54]. Recently, Gamaniel et al. [55] have studied the influence of polymers in cavitating contacts by using a linearized model. However, we have shown that such models are not accurate beyond a small range of Wi. Therefore, one may require the proposed VR to investigate cavitation for polymeric lubricants at large values of the Weissenberg number.

Declaration of competing interest

The authors declare that they have no known competing financial interests or personal relationships that could have appeared to influence the work reported in this paper.

Acknowledgments

The authors would like to acknowledge the Turkish National Research Agency (TÜBİTAK) for supporting this work under the project 117M434. We would like to thank the editor Prof. Ian Frigaard for the useful discussion about the validity of the boundary conditions.

Appendix A. Numerical stability under the thin film approximation

The criteria for numerical stability of the Oldroyd-B constitutive relation is provided in Ref. [56]. Particularly two conditions must be satisfied by the tensor $\boldsymbol{C} = -\frac{1}{2\lambda}\mathbf{I} + \mathbf{L}$

$$\mathrm{tr}(\boldsymbol{C}) = -\frac{1}{\lambda} < 0 \quad \text{and} \tag{42a}$$

$$\det(\boldsymbol{C}) = \frac{1}{4\lambda^2} - d^2 + \omega^2 < 0, \tag{42b}$$

where the parameters $d^2 = -\det(\mathbf{L}+\mathbf{L}^T)/4$ and $\omega^2 = \det(\mathbf{L}-\mathbf{L}^T)/4$ are functions of the velocity gradient tensor $\mathbf{L}$ and its transpose $\mathbf{L}^T$. It is clear that $\det(\boldsymbol{C})$ is determined only by the velocity gradient tensor [18]. While Eq. (42a) is always satisfied, we need to check the validity of Eq. (42b).

By using Eq. (2), we can find $\mathbf{L}+\mathbf{L}^T$ and $\mathbf{L}-\mathbf{L}^T$ under the thin film assumption

$$\begin{aligned}\mathbf{L}+\mathbf{L}^T &= \frac{U}{\ell}\begin{Bmatrix} 2\frac{\partial u}{\partial x} & \frac{1}{\epsilon}\frac{\partial u}{\partial y} + \epsilon\frac{\partial v}{\partial x} \\ \frac{1}{\epsilon}\frac{\partial u}{\partial y} + \epsilon\frac{\partial v}{\partial x} & 2\frac{\partial v}{\partial y}\end{Bmatrix} \quad \text{and} \\ \mathbf{L}-\mathbf{L}^T &= \frac{U}{\ell}\begin{Bmatrix} 0 & \frac{1}{\epsilon}\frac{\partial u}{\partial y} - \epsilon\frac{\partial v}{\partial x} \\ -\frac{1}{\epsilon}\frac{\partial u}{\partial y} + \epsilon\frac{\partial v}{\partial x} & 0\end{Bmatrix}.\end{aligned} \tag{43}$$

As a result d^2 and ω^2 are

$$d^2 = -\frac{\ell}{4U}\left(4\frac{\partial u}{\partial x}\frac{\partial v}{\partial y} - \left[\frac{1}{\epsilon}\frac{\partial u}{\partial y} + \epsilon\frac{\partial v}{\partial x}\right]^2\right) \quad \text{and} \tag{44a}$$

$$\omega^2 = \frac{\ell}{4U}\left[\frac{1}{\epsilon}\frac{\partial u}{\partial y} - \epsilon\frac{\partial v}{\partial x}\right]^2, \tag{44b}$$

respectively. Upon simplification, the difference $\omega^2 - d^2$ is given as

$$\omega^2 - d^2 = \frac{\ell}{U}\left(\frac{\partial u}{\partial x}\frac{\partial v}{\partial y} - \frac{\partial u}{\partial y}\frac{\partial v}{\partial x}\right), \tag{45}$$

which is independent of ϵ. This is also intuitively observed from Eqs. (3d)–(3f), which do not simplify after the thin film approximation and retains the numerically problematic convective–derivative. In conclusion, the lubrication approximation does not induce any numerical stability and the solution of Eqs. (3d)–(3f) will incur in the HWNP as well. Note also that the HWNP is caused by a restriction on the minimum grid spacing due to a polynomial approximation of the Oldroyd-B, see Section 2.4. This restriction is greatly relaxed via the LCR but not entirely eliminated [16]. Therefore, we should still expect a numerical failure at high Wi also for the thin film equations solved by a LCR.

Appendix B. VR equation derivation

The viscoelastic Reynolds equation follows the same steps of the classical Reynolds equation. However, we make no attempt to remove the integrals similar to the derivation of GR [25]. We integrate the thin film momentum equation (Eq. (3b)) twice along the film thickness to obtain

$$\frac{dp}{dx}\frac{y^2}{2} + c_1 y + c_2 = (1-\beta)u + \int_0^y \tau_{xy}dy + \int_0^y\int_0^y \frac{\partial \tau_{xx}}{\partial x}dy'dy. \tag{46}$$

If we apply the boundary conditions, $u = 1$ at $y = 0$ and $u = 0$ at $y = h$, we get

$$c_1 = -\frac{h}{2}\frac{dp}{dx} + \frac{1}{h}\left(\int_0^y \tau_{xy}dy + \int_0^y\int_0^y \frac{\partial \tau_{xx}}{\partial x}dy' - \beta\right), \quad \text{and} \quad c_2 = \beta. \tag{47}$$

The velocity field is obtained by substituting the integration constants (Eq. (47)) into Eq. (46)

$$\begin{aligned}u = \frac{1}{2\beta}\frac{dp}{dx}(y^2 - yh) + \left(1 - \frac{y}{h}\right) + \frac{1}{\beta}\left(\frac{y}{h}\int_0^h \tau_{xy}dy - \int_0^y \tau_{xy}dy'\right) \\ + \frac{1}{\beta}\left(\frac{y}{h}\int_0^h\int_0^y \frac{\partial \tau_{xx}}{\partial x}dy'dy - \int_0^y\int_0^y \frac{\partial \tau_{xx}}{\partial x}dy'dy\right).\end{aligned} \tag{48}$$

To obtain the VR equation we substitute the velocity field into the continuity Eq. (3a), apply the Leibnitz theorem and simplify by noting that the $v = 0$ at the walls

$$\frac{\partial}{\partial x}\int_0^h u dy + \frac{dh}{dx}u|_{y=h} + v|_{y=h} - v|_{y=0} = 0. \tag{49}$$

After integrating over the channel height the VR equation is obtained

$$\begin{aligned}\frac{d}{dx}\left(\frac{h^3}{12}\frac{dp}{dx}\right) = \frac{\beta}{2}\frac{dh}{dx} + \frac{d}{dx}\Bigg(\int_0^h \frac{y}{h}\int_0^h\int_0^y \frac{d\tau_{xx}}{dx}dy''dy'dy \\ - \int_0^h\int_0^y\int_0^y \frac{d\tau_{xx}}{dx}dy''dy'dy\Bigg) \\ + \frac{d}{dx}\left(\int_0^h \frac{y}{h}\int_0^h \tau_{xy}dy'dy - \int_0^h\int_0^y \tau_{xy}dy'dy\right).\end{aligned} \tag{50}$$

Appendix C. Polynomial approximation and discretization of the viscoelastic stresses

The stress polynomials are written in terms of the unknown functions of $T_{ij}^{(k)}(x,t)$. If we choose to evaluate the polynomials at a chosen y, each $T_{ij}^{(n)}$ can be expressed in terms of the stress

$$\tau_{xx}(x,y,t) = T_{xx}^{(I)}(x,t) + T_{xx}^{(II)}(x,t)y + T_{xx}^{(III)}(x,t)y^2 + T_{xx}^{(IV)}(x,t)y^3, \tag{51a}$$

$$\tau_{xy}(x,y,t) = T_{xy}^{(I)}(x,t) + T_{xy}^{(II)}(x,t)y + T_{xy}^{(III)}(x,t)y^2 + T_{xy}^{(IV)}(x,t)y^3 + T_{xy}^{(V)}(x,t)y^4, \text{ and} \tag{51b}$$

$$\tau_{yy}(x,y,t) = T_{yy}^{(I)}(x,t) + T_{yy}^{(II)}(x,t)y + T_{yy}^{(III)}(x,t)y^2 + T_{yy}^{(IV)}(x,t)y^3 + T_{yy}^{(V)}(x,t)y^4, \tag{51c}$$

For instance, if we want to determine $\tau_{xx}(x,y,t)$ at equidistant stencils, i.e. $y = \{0,\ h/3,\ 2h/3,\ h\}$, then the unknown coefficients for $\tau_{xx}(x,y,t)$ are

$$T_{xx}^{(I)} = \tau_{xx}^{(0)}, \tag{52a}$$

$$T_{xx}^{(II)} = \frac{1}{2h}\left(-11\tau_{xx}^{(0)} + 18\tau_{xx}^{(h/3)} - 9\tau_{xx}^{(2h/3)} + 2\tau_{xx}^{(h)}\right), \tag{52b}$$

$$T_{xx}^{(II)} = \frac{9}{2h}\left(2\tau_{xx}^{(0)} - 5\tau_{xx}^{(h/3)} + 4\tau_{xx}^{(2h/3)} - \tau_{xx}^{(h)}\right), \text{ and} \tag{52c}$$

$$T_{xx}^{(IV)} = \frac{9}{2h}\left(-\tau_{xx}^{(0)} + 3\tau_{xx}^{(h/3)} - 3\tau_{xx}^{(2h/3)} + \tau_{xx}^{(h)}\right), \tag{52d}$$

where $\{\tau_{xx}^{(0)}, \tau_{xx}^{(h/3)}, \tau_{xx}^{(2h/3)}, \tau_{xx}^{(h)}\}$ are the normal stresses at the stencil locations. We can determine $\tau_{xx}^{(k)}(x,y,t)$ by writing explicit equations for the four stencil points.

Similarly for τ_{xy}, by choosing an equidistant stencil, i.e. $y = \{0,\ h/4,\ h/2,\ 3h/4,\ h\}$,

$$T_{xy}^{(I)} = \tau_{xy}^{(0)}, \tag{53a}$$

$$T_{xy}^{(II)} = \frac{1}{210h}\left(-1435\tau_{xy}^{(0)} + 1920\tau_{xy}^{(h/4)} - 9\tau_{xy}^{(h/2)} - 896\tau_{xy}^{(3h/4)} + 420\tau_{xx}^{(h)}\right), \tag{53b}$$

$$T_{xy}^{(III)} = \frac{1}{210h}\left(2905\tau_{xy}^{(0)} - 5440\tau_{xy}^{(h/4)} + 57\tau_{xy}^{(h/2)} + 4928\tau_{xy}^{(3h/4)} + -2450\tau_{xx}^{(h)}\right), \tag{53c}$$

$$T_{xy}^{(IV)} = \frac{16}{105h}\left(-70\tau_{xy}^{(0)} + 150\tau_{xy}^{(h/4)} - 3\tau_{xy}^{(h/2)} - 182\tau_{xy}^{(3h/4)} + 105\tau_{xx}^{(h)}\right), \text{ and} \tag{53d}$$

$$T_{xy}^{(V)} = \frac{8}{105h}\left(35\tau_{xy}^{(0)} - 80\tau_{xy}^{(h/4)} + 3\tau_{xy}^{(h/2)} + 112\tau_{xy}^{(3h/4)} - 70\tau_{xy}^{(h)}\right). \tag{53e}$$

The equations for the coefficient functions $\tau_{yy}^{(k)}$ are identical to those appearing in τ_{xy}, since we chose to use the (i) same stencil and (ii) the 4th degree polynomial approximation. Finally, we substitute Eqs. (52) and (53) at the chosen film locations into the thin film equations (Eqs. (3d)–(3f)) and solve for the coefficient functions that depend only on x and t.

Below, we show the discretization for each stress component at $y = 0$,

$$\tau_{xx}^{(0)}|_i^{t+\Delta t} = \frac{1}{\epsilon Wi}\left(-\tau_{xx}^{(0)}|_i^t\right) - \Delta t\left(\frac{\tau_{xx}^{(0)}|_i^t - \tau_{xx}^{(0)}|_{i-1}^t}{\Delta x} - 2\frac{\partial u}{\partial y}\Big|_i \tau_{xy}^{(0)}|_i^t - 2\frac{\partial u}{\partial x}\Big|_i \tau_{xx}^{(0)}|_i^t\right) + \tau_{xx}^{(0)}|_i^t, \tag{54a}$$

$$\tau_{xy}^{(0)}|_i^{t+\Delta t} = \frac{1}{\epsilon Wi}\left((1-\beta)\frac{\partial u}{\partial y}\Big|_i - \tau_{xy}^{(0)}|_i^t\right) - \Delta t\left(\frac{\tau_{xy}^{(0)}|_i^t - \tau_{xy}^{(0)}|_{i-1}^t}{\Delta x} - \frac{\partial u}{\partial y}\Big|_i \tau_{yy}^{(0)}|_i^t - \frac{\partial v}{\partial x}\Big|_i \tau_{xx}^{(0)}|_i^t\right) + \tau_{xy}^{(0)}|_i^t, \tag{54b}$$

$$\tau_{yy}^{(0)}|_i^{t+\Delta t} = \frac{1}{\epsilon Wi}\left(2(1-\beta)\frac{\partial v}{\partial y}\Big|_i - \tau_{yy}^{(0)}|_i^t\right) - \Delta t\left(\frac{\tau_{yy}^{(0)}|_i^t - \tau_{yy}^{(0)}|_{i-1}^t}{\Delta x} - \frac{\partial v}{\partial y}\Big|_i \tau_{yy}^{(0)}|_i^t - \frac{\partial v}{\partial x}\Big|_i \tau_{xy}^{(0)}|_i^t\right) + \tau_{yy}^{(0)}|_i^t, \tag{54c}$$

where Δt is the time step and Δx is the grid spacing. Similarly, we have to write explicit equations for the remaining film locations. Note, however, that the spatial derivatives (d/dx and d/dy) do not vanish for the interior film locations. Additionally, note that for $Wi = 0$, Eqs. (54a)–(54c) cannot be solved due to the presence of Wi in the denominator. For values of $Wi \ll 1$, time-integration via the explicit Euler scheme causes a significant delay in arriving to the steady state solution. However, the solution for such cases may not be required, since the solutions are indistinguishable from the Newtonian case.

References

[1] B.J. Hamrock, S.R. Schmid, B.O. Jacobson, Fundamentals of Fluid Film Lubrication, CRC Press, 2004.
[2] A.Z. Szeri, Fluid Film Lubrication, Cambridge University Press, 2010.
[3] F. Ree, T. Ree, H. Eyring, Relaxation theory of transport problems in condensed systems, Ind. Eng. Chem. 50 (7) (1958) 1036–1040.
[4] S. Bair, W.O. Winer, A rheological model for elastohydrodynamic contacts based on primary laboratory data, J. Lubr. Technol. 101 (3) (1979) 258–264.
[5] N. Phan-Thien, H. Low, Squeeze-film flow of a viscoelastic fluid a lubrication model, J. Non-Newton. Fluid Mech. 28 (2) (1988) 129–148.
[6] B. Williamson, K. Walters, T. Bates, R. Coy, A. Milton, The viscoelastic properties of multigrade oils and their effect on journal-bearing characteristics, J. Non-Newton. Fluid Mech. 73 (1–2) (1997) 115–126.
[7] S. Bair, F.E. Lockwood, W.B. Anderson, Z. Zhang, D. Dotson, Measurements of elasticity in multigrade motor oil at elevated pressure, Tribol. Trans. 50 (3) (2007) 407–414.
[8] S. Bair, The first normal stress difference in a shear-thinning motor oil at elevated pressure, Tribol. Trans. 58 (4) (2015) 654–659.
[9] K. Walters, The motion of an elastico-viscous liquid contained between coaxial cylinders (II), Quart. J. Mech. Appl. Math. 13 (4) (1960) 444–461.
[10] N. Phan-Thien, R.I. Tanner, A new constitutive equation derived from network theory, J. Non-Newton. Fluid Mech. 2 (4) (1977) 353–365.
[11] R.I. Tanner, S. Nasseri, Simple constitutive models for linear and branched polymers, J. Non-Newton. Fluid Mech. 116 (1) (2003) 1–17.
[12] H.R. Warner Jr., Kinetic theory and rheology of dilute suspensions of finitely extendible dumbbells, Ind. Eng. Chem. Fundam. 11 (3) (1972) 379–387.
[13] R. Bird, P. Dotson, N. Johnson, Polymer solution rheology based on a finitely extensible bead—spring chain model, J. Non-Newton. Fluid Mech. 7 (2–3) (1980) 213–235.
[14] M.R. Jovanović, S. Kumar, Nonmodal amplification of stochastic disturbances in strongly elastic channel flows, J. Non-Newton. Fluid Mech. 166 (14–15) (2011) 755–778.
[15] L. Biancofiore, L. Brandt, T.A. Zaki, Streak instability in viscoelastic Couette flow, Phys. Rev. Fluids 2 (4) (2017) 043304.
[16] R. Fattal, R. Kupferman, Constitutive laws for the matrix-logarithm of the conformation tensor, J. Non-Newton. Fluid Mech. 123 (2–3) (2004) 281–285.
[17] R. Fattal, R. Kupferman, Time-dependent simulation of viscoelastic flows at high Weissenberg number using the log-conformation representation, J. Non-Newton. Fluid Mech. 126 (1) (2005) 23–37.
[18] M.A. Hulsen, R. Fattal, R. Kupferman, Flow of viscoelastic fluids past a cylinder at high Weissenberg number: stabilized simulations using matrix logarithms, J. Non-Newton. Fluid Mech. 127 (1) (2005) 27–39.
[19] H. Jasak, A. Jemcov, Z. Tukovic, et al., OpenFOAM: A C++ library for complex physics simulations, in: International Workshop on Coupled Methods in Numerical Dynamics, Vol. 1000, IUC Dubrovnik Croatia, 2007, pp. 1–20.
[20] F. Habla, M.W. Tan, J. Haßlberger, O. Hinrichsen, Numerical simulation of the viscoelastic flow in a three-dimensional lid-driven cavity using the log-conformation reformulation in OpenFOAM®, J. Non-Newton. Fluid Mech. 212 (2014) 47–62.
[21] D. Dowson, A generalized Reynolds equation for fluid-film lubrication, Int. J. Mech. Sci. 4 (2) (1962) 159–170.
[22] J. Tevaarwerk, K. Johnson, A simple non-linear constitutive equation for elastohydrodynamic oil films, Wear 35 (2) (1975) 345–356.
[23] K.L. Johnson, J. Tevaarwerk, Shear behaviour of elastohydrodynamic oil films, Proc. R. Soc. Lond. Ser. A Math. Phys. Eng. Sci. 356 (1685) (1977) 215–236.
[24] Y. Peiran, W. Shizhu, A generalized Reynolds equation for non-Newtonian thermal elastohydrodynamic lubrication, J. Tribol. 112 (4) (1990) 631–636.
[25] R. Wolff, A. Kubo, A generalized non-Newtonian fluid model incorporated into elastohydrodynamic lubrication, J. Tribol. 118 (1) (1996) 74–82.
[26] R.S. Paranjpe, Analysis of non-Newtonian effects in dynamically loaded finite journal bearings including mass conserving cavitation, J. Tribol. 114 (4) (1992) 736–744.
[27] F.T. Akyildiz, H. Bellout, Viscoelastic lubrication with Phan–Thein–Tanner fluid (PTT), J. Tribol. 126 (2) (2004) 288–291.
[28] J.A. Tichy, Non-Newtonian lubrication with the convected Maxwell model, J. Tribol. 118 (2) (1996) 344–348.
[29] R. Zhang, X.K. Li, Non-Newtonian effects on lubricant thin film flows, J. Eng. Math. 51 (1) (2005) 1.
[30] R. Zhang, X. He, S.X. Yang, X. Li, Perturbation solution of non-Newtonian lubrication with the convected Maxwell model, J. Tribol. 127 (2) (2005) 302–305.
[31] X.K. Li, Y. Luo, Y. Qi, R. Zhang, On non-newtonian lubrication with the upper convected Maxwell model, Appl. Math. Model. 35 (5) (2011) 2309–2323.
[32] X.K. Li, Non-Newtonian effects on lubricant thin film flows, J. Cent. South Univ. Technol. 14 (1) (2007) 68–72.
[33] X.K. Li, Non-Newtonian lubrication with the Phan–Thien–Tanner model, J. Eng. Math. 87 (1) (2014) 1–17.
[34] Y.L. Zhang, O.K. Matar, R.V. Craster, Surfactant spreading on a thin weakly viscoelastic film, J. Non-Newton. Fluid Mech. 105 (1) (2002) 53–78.

[35] S. Saprykin, R.J. Koopmans, S. Kalliadasis, Free-surface thin film flows over topography: influence of inertia and viscoelasticity, J. Fluid Mech. 578 (2007) 271.
[36] R.I. Tanner, Increase of bearing loads due to large normal stress differences in viscoelastic lubricants, J. Appl. Mech. 36 (3) (1969) 634–635.
[37] J. Tichy, B. Bou-Saïd, The Phan–Thien and Tanner model applied to thin film spherical coordinates: applications for lubrication of hip joint replacement, J. Biomech. Eng. 130 (2) (2008).
[38] W.G. Sawyer, J.A. Tichy, Non-Newtonian lubrication with the second-order fluid, J. Tribol. 120 (3) (1998) 622–628.
[39] F. Pimenta, M. Alves, Stabilization of an open-source finite-volume solver for viscoelastic fluid flows, J. Non-Newton. Fluid Mech. 239 (2017) 85–104.
[40] A. Beris, R. Armstrong, R. Brown, Finite element calculation of viscoelastic flow in a journal bearing: II. Moderate eccentricity, J. Non-Newton. Fluid Mech. 19 (3) (1986) 323–347.
[41] R. Keunings, A survey of computational rheology, in: Proceedings of the XIIIth International Congress on Rheology, Vol. 1, British Soc. Rheol, 2000, pp. 7–14.
[42] W.L. Briggs, V.E. Henson, S.F. McCormick, A Multigrid Tutorial, SIAM, 2000.
[43] H. Jasak, Error Analysis and Estimation for the Finite-Volume Method with Applications to Fluid Flows (Ph.D. thesis), University of London, 1996, p. 396.
[44] S.C. Xue, R. Tanner, N. Phan-Thien, Numerical modelling of transient viscoelastic flows, J. Non-Newton. Fluid Mech. 123 (1) (2004) 33–58.
[45] C. Fernandes, M. Araujo, L. Ferrás, J.M. Nóbrega, Improved both sides diffusion (iBSD): A new and straightforward stabilization approach for viscoelastic fluid flows, J. Non-Newton. Fluid Mech. 249 (2017) 63–78.
[46] R.M. Mortier, S.T. Orszulik, M.F. Fox, Chemistry and Technology of Lubricants, Vol. 107115, Springer, 2010.
[47] R.I. Tanner, Engineering Rheology, Vol. 52, OUP Oxford, 2000.
[48] N. Phan-Thien, N. Mai-Duy, Understanding Viscoelasticity: An Introduction to Rheology, Springer, 2017.
[49] R. Boncompain, M. Fillon, J. Frene, Analysis of thermal effects in hydrodynamic bearings, J. Tribol. 108 (2) (1986) 219–224.
[50] D. Dowson, J. Dunn, C. Taylor, The piezo-viscous fluid, rigid solid regime of lubrication, Proc. Inst. Mech. Eng. C 197 (1) (1983) 43–52.
[51] T. Almqvist, R. Larsson, Some remarks on the validity of Reynolds equation in the modeling of lubricant film flows on the surface roughness scale, J. Tribol. 126 (4) (2004) 703–710.
[52] J.K. Schuh, R.H. Ewoldt, Low Reynolds number friction reduction with polymers and textures, J. Non-Newton. Fluid Mech. 273 (2019) 104167.
[53] D. Dowson, C.M. Taylor, Cavitation in bearings, Annu. Rev. Fluid Mech. 11 (1) (1979) 35–65.
[54] L. Biancofiore, M. Giacopini, D. Dini, Interplay between wall slip and cavitation: A complementary variable approach, Tribol. Int. 137 (2019) 324–339.
[55] S. Gamaniel, D. Dini, L. Biancofiore, The effect of fluid viscoelasticity in lubricated contacts in the presence of cavitation, Tribology International (2021) 107011.
[56] J. Van Der Zanden, M. Hulsen, Mathematical and physical requirements for successful computations with viscoelastic fluid models, J. Non-Newton. Fluid Mech. 29 (1988) 93–117.